This is a preprint, the final version is subject to change, of the American Mineralogist (MSA)
Cite as Authors (Year) Title. American Mineralogist, in press.
(DOI will not work until issue is live.) DOI: http://dx.doi.org/10.2138/am-2017-5998

Cu-Mo partitioning between felsic melts and saline-aqueous fluids as a function of X_{NaCleq}, fO_2 and fS_2

Brian C. Tattitch[1*] and Jon D. Blundy[1]

[1] University of Bristol, School of Earth Sciences, Wills Memorial Building, Bristol BS8 1RJ,UK

REVISION 1

ABSTRACT

The formation of porphyry Cu-Mo deposits hinges critically on the ability of an exsolving magmatic volatile phases (MVP) to efficiently extract the available Cu and Mo from the silicate melt and transport them to the site of mineralization. There has been substantial debate about the relative importance of the critical parameters likely to control metal partitioning amongst silicate melts and supercritical fluids, vapors and brines. To explore the relative contributions of key MVP parameters (X_{NaCleq}, fO_2, fS_2) we present felsic magmatic Cu-Mo partitioning experiments at both reduced (NNO+0.6) and oxidized conditions (fO_2=NNO+2), at high fS_2, and over the full range of salinities (X_{NaCleq}) relevant to porphyry deposit formation. The experiments demonstrate that fluid-melt Cu partition coefficients ($D_{Cu}^{f/m}$) have a dominantly 2nd-order exponential relationship with X_{NaCleq} at relevant salinities, consistent with a (Na,K)$CuCl_2$ ion-pair complexation mechanism. We find a strong linear dependence of Cu partitioning on Cl partitioning between coexisting brine and vapor, in good agreement with limited data from unmodified natural fluid inclusions. Whereas H_2S can increase Cu partitioning via (Na,K)CuCl(HS) formation, SO_2 has no measureable effect on Cu partitioning. These data allow for quantifying the strong partitioning of Cu and Mo out of silicate melts at

MVP salinities above ~5wt%, which will become further enriched into tardo-magmatic brines on phase separation. Our data also highlight that low-salinity (< 2-3 wt% $NaCl_{eq}$) oxidized MVPs are not capable of compatibly extracting Cu from evolved silicate melts or transporting it to the site of mineralization. We also show that $D_{Mo}^{f/m}$ is a linear function of X_{NaCleq}, consistent with mono-chloride (e.g. {Na,K}MoO_3Cl), Na-K molybdate (e.g. {Na,K}$HMoO_4$), or thio-molybdate ({Na,K}$HMoO_2S_2$) complexation mechanisms at modest salinities (>3wt%) rather than the Mo-oxy-hydroxy ($MoO_2(OH)_2$) complexation observed at lower salinities. The fO_2 of the magmatic system has a subordinate effect on $D_{Mo}^{f/m}$, with enhanced partitioning at higher fO_2.

We use the combined dataset to produce expressions for $D_{Cu}^{f/m}$ and $D_{Mo}^{f/m}$ as functions of X_{NaCleq}, X_{H2S}, and fO_2:

$D_{Cu}^{f/m} = 8.0(\pm1.4)\text{x}10^4\ [(X_{NaCleq})^2(X_{H2O})^{14\pm2}\{1+180(\pm60)(X_{H2S})\}] + 380(\pm50)(X_{NaCleq}) +$ $0.8(\pm0.5)$ and $D_{Mo}^{f/m}(\text{at NNO+2}) = 430(\pm60)*(X_{NaCleq}) + 1.5(\pm0.7)*(X_{H2O})$

These equations provide Cu-Mo fluid-melt partition coefficients for common arc melt-MVP assemblages as their composition evolves through time and space. Quantitative modelling of the contrasting partitioning behavior of Cu and Mo using these equations will allow for significant improvement in understanding metal extraction and porphyry deposit formation.

INTRODUCTION

A critical step in the formation of porphyry-style ore deposits is the efficient extraction of ore metals (e.g. Cu, Mo, Au, Ag) from arc magmas during exsolution of

45 magmatic volatile phases (MVPs)[1]. These volatile phases represent the precursor or
46 "proto-ore fluids" (Candela et al. 2010) that must leave the magmatic hearth, enter fluid-
47 focusing zones and react with other volatile phases and host rock to eventually generate
48 the hydrothermally altered, hypogene sulfide ore zones characteristic of porphyry
49 deposits (e.g. Sillitoe, 2010; Sinclair 2007). Advances in magmatic-hydrothermal
50 experiments and techniques for fluid inclusion analysis have enhanced our understanding
51 of the physical and chemical properties of these MVPs and their influence on the
52 extraction of different metals. Those experiments have focused on increasingly
53 challenging aspects of simulating volatile partitioning, specifically the role of salinity
54 (Candela and Holland 1984, Williams et al. 1995), the impact of the sulfur and fS_2
55 (Frank et al. 2011; Simon et al. 2006), the role of CO_2 (Tattitch et al. 2015) and on
56 thermodynamic modelling of the complexes which control metal speciation in high
57 temperature fluids (Zajacz et al. 2011). Finally, diffusion studies of quartz
58 (Lerchbaumber and Audétat 2012; Zajacz et al. 2009) and careful evaluation of fluid
59 inclusions from ore deposits (Seo and Heinrich 2013) highlight the need for caution when
60 making interpretations of the high temperature partitioning of Cu and other small, fast-
61 diffusing monovalent cations. The revelation that Cu can diffuse into low-salinity fluid
62 inclusions in natural systems (Lerchbaumer and Audétat 2012; Seo and Heinrich 2013)
63 demands we avoid using such inclusions to infer that Cu partitioning would favour

[1] This process is often referred to informally as "degassing" in the petrological literature. We use the two terms interchangeably here.

vapors over brines[2]. Instead we must focus on magmatic volatile experimental work that is not subject to the types of post-entrapment complications that limit interpretations of natural fluid inclusions.

Ore-metal focused experimental studies have been complemented by numerous advances in our understanding of arc magma generation (e.g. Annen et al. 2006; Cashman and Blundy 2000; Lee et al. 2012; Sisson and Grove 1993; Sisson et al. 2005), the exchange of major volatile components (H_2O, CO_2, H_2S, SO_2, Cl) between melts and volatile phases (e.g. Lowenstern 2000, 2001; Webster 1997; Webster et al. 2011; Ghiorso & Gualda 2015), and the physical properties of the MVPs themselves (Bodnar et al. 1985; Sun and Dubessy 2012). Given our improved understanding of arc magma generation and degassing, the most obvious goal is to evaluate the *where*, *when* and *how much* for the extraction of ore metals to constrain the input of proto-ore fluids that leads to the formation of Mo-Cu, Cu-Mo, Cu-Au porphyry copper deposits (PCD) as well as other related hydrothermal deposits (e.g. epithermal). Yet, the systematic application of experimental results to understanding ore metal partitioning has been limited by the the relative paucity of partitioning data (compared to mineral-melt systems) and an incomplete picture of MVPs and their evolving chemical characteristics during magma ascent and crystallization.

In order to understand the extraction of copper from magmas for the wide range of exsolution conditions predicted for porphyry-style ore deposits, we present a compilation of the existing data for copper partitioning, as well as new experiments

[2] We use "brine" to denote a hypersaline fluid that is immiscible with a coexisting low-salinity vapor below the solvus in the H_2O-$NaCl_{eq}$ system at the P-T conditions of interest.

exploring several thermodynamic vectors (T, P, X_{NaCleq} fH_2S/fSO_2). These data are unified by framing the effects of their thermodynamic variability in terms of the dominant control on copper partitioning, namely the total chloride concentration of an exsolved aqueous fluid ($\sum$Cl), as expressed in terms of NaCl-equivalent units ($NaCl_{eq}$) of the MVPs. This statement is founded on numerous studies that demonstrate that when chlorine is available for metal complexing, the partitioning of copper among silicate melts, vapors, brines and supercritical fluids follows the salinity of the MVPs and chlorine concentration of the melt (Candela and Holland 1984; Candela and Piccoli 1995; Candela and Piccoli 2005; Frank et al. 2003; Simon et al. 2006; Tattitch et al. 2015; Williams et al. 1995). After placing the experiments within this $\sum$Cl framework, we can then examine the subordinate effects of sulfur species that may also be present in proto-ore fluids and the overall redox state, as expressed as the oxygen fugacity (fO_2).

Whereas the dataset for copper partitioning is fairly robust, the data for molybdenum partitioning are significantly less developed. Nearly all PCD show some degree of Mo enrichment in the ore zones. However, the diversity of Mo, Cu and Au grades has led to classification of PCD according to their relative enrichments (i.e. Cu-Mo, Mo-Cu, Cu, Cu-Au). In PCD with appreciable Mo and Cu the distribution of the Mo ore (dominantly molybdenite) and that of Cu are often decoupled (John et al. 2010; Redmond et al. 2004; Rusk et al. 2008; Sillitoe 2010), indicating that a different set of MVP properties may control the extraction, complexation and or mineralization of Mo. This challenge for understanding PCD mineralization led, early on, to experiments aimed at unravelling the independent partitioning behaviour of Mo compared to Cu.

The first quantitative experimental work is the analysis of supercritical fluids by Candela and Holland (1984), which provided a basic understanding of Mo partitioning between melt and fluid at magmatic conditions, concluding that, unlike for Cu, Mo partitioning had no dependence on fluid salinity. However, these early experiments relied upon analysis of quenched fluids, which may not preserve the elevated Mo and/or Cu concentrations of the more saline magmatic MVPs. Later work of Ulrich and Mavrogenes (2008) examined the solubility of Mo species in MVPs ranging from ∑Cl of zero to nearly 4 M (~20wt% $NaCl_{eq}$), using chemical analysis of synthetic fluid inclusions. Their study highlights a mild salinity dependence trend, consistent with a roughly 1:1 ratio for Mo:Cl in the metal complexes present in MVPs. However, this work involved sulfur-free starting composition, precluding molybdenite saturation and leading to unusually high Mo concentrations. Moreover, it did not examine changing fO_2, or equilibrium of the fluid with a silicate melt. Without these critical aspects, models for Mo extraction and mineralization have remained much more poorly constrained than those for Cu. This leaves us with two questions: (i) does Cl form part of the dominant Mo complexes that occur in sulfurous magmatic fluids; and (ii) does fO_2 play a role in the stability of those complexes? Thus, our goals for Mo mirror those for Cu. We must explore simultaneously the influence of fS_2, fO_2 and ∑Cl on both Cu and Mo partitioning in order to provide a more complete narrative for what controls the extraction of these metals from silicate melts and, ultimately, their accumulation in PCDs.

Sulfur in Porphyry Copper Deposits

Porphyry copper deposits can be described as giant sulfur anomalies with variable metal endowments of Fe, Cu, Mo and Au. The relative abundance of each of these metals and their different affinities for MVPs and melts relative to sulfur species is critical in PCD formation. Observations from the hypogene (magmatic) ore zones of PCD show that Cu and Mo are hosted almost exclusively in sulfide minerals. Thus the precipitation of Cu and Mo as sulfides points to the possibility that sulfur ligands (e.g. HS^-) play a role in deposition, and possibly transport, under hydrothermal conditions (Audétat et al. 1998; Heinrich 2005; Heinrich et al. 2004; Heinrich et al. 1999; Pettke et al. 2010; Pokrovski et al. 2008; Rusk et al. 2004; Ulrich et al. 1999). Studies of fluid inclusions from the ore zone suggest that the chloride content of many fluid inclusions is insufficient to balance the solute load, which is often used to infer a role for other ligands, including HS^-, in transporting ore metals (Heinrich et al. 1992; Simon et al. 2006).

Sulfur isotopic data from porphyry deposits supports a magmatic source for the mineralizing sulfur, and many believe it is sourced from the same MVPs that extract the ore metals. Recent studies of $\delta^{34}S$ systematics of sulfides from porphyry deposits including Bingham, Butte, and Lepanto Far Southeast, are consistent with a magmatic origin for the sulfur (Field et al. 2005; Hattori and Keith 2001; Imai 2000; Simon and Ripley 2011). Here again, many infer that the sulfur, which is certainly sourced from associated arc magmas, plays an important role in transport of ore metals and the formation of sulfide mineralization, though this is not definitive. In addition, several observations challenge whether sulfide mineralization is a consequence of sulfur-complexed metal transport.

Hattori and Keith (2001) discuss that, given the mass balance considerations of the small, evolved intrusions and their H_2O and S contents, a much larger (mafic) sulfur reservoir is required to account for the large sulfur anomaly of a PCD. However, numerous studies have shown that the partitioning of Cu into magmatic sulfide relative to the parental melt is even more dramatic than into MVPs, with $D_{Cu}^{Sulfide/melt} > 1000$ at all magmatic conditions (e.g. Jugo et al. 1999; Matjuschkin et al. 2016; Ripley et al. 2002). As a result, if a magma saturates with even 0.1 mass% of an Fe (±Cu) sulfide phase prior to volatile saturation, then 50% or more of all the Cu present in the melt will be sequestered in the sulfide phase (Audétat and Simon 2012; Jugo et al. 1999; Simon et al. 2006). Given this intense partitioning, early sulfide saturation during differentiation, prior to exsolution of MVPs, is often referred to as "poisoning" the system, and is thought to greatly reduce the potential for ore deposit formation unless these sulfides can be destroyed and release their metal contents to ascending fluids (Audétat and Simon 2012; Candela and Piccoli 2005; Jugo et al. 1999; Lynton et al. 1993; Mengason et al. 2010; Nadeau et al. 2010; Sillitoe 2010; Simon and Ripley 2011).

Keeping in mind the potential perils of early sulfide saturation, many studies highlight that the intrusions associated with arc magmas are oxidized (>NNO) resulting in a dominance of S^{4+} and S^{6+} rather than S^{2-} in their magmatic sulfur budgets (e.g. Audétat and Simon 2012; Ballard et al. 2002; Candela and Piccoli 2005; Sillitoe 2010; Simon and Ripley 2011; Streck and Dilles 1998). A highly oxidized system might then be expected to avoid early sulfide saturation by keeping the proportion of S^{2-} in the melt relatively low even at high total sulfur content. Yet recent work by Matjuschkin et al. (2016) has questioned whether arc magmas can avoid sulfide saturation in the lower crust

174 simply by being very oxidized. They demonstrate that the sulfide/sulfate transition for
175 magmas moves to much higher fO_2 values at 5-15 kbar (~NNO+4) compared to studies
176 at ≤2 kbar (Botcharnikov et al. 2011; Carroll and Rutherford 1985; Clemente et al 2004;
177 Jugo et al. 2010). They suggest that arc magmas may avoid sulfide saturation through
178 other mechanisms such as early depletion of sulfur through degassing, which further
179 complicates the issue of generating a single shallow, evolved, Cu-Cl-S-rich magma.
180 In light of these challenges Blundy et al (2015) proposed and tested
181 experimentally an alternative mechanism by which ore metals might be extracted from
182 evolved melts via Cl-rich fluids that are subsequently mineralized by fluxing of sulfurous
183 gases from deeper, mafic reservoirs. This model for PCD formation does not require the
184 metal-chloride fluid to be sourced from the same magma as the abundant sulfur required
185 for mineralization; in effect metal supply and sulfur supply are decoupled. A recent study
186 by Henley et al. (2015) discussed an alterative mechanism whereby an oxidized sulfurous
187 gas (SO_2 dominant) reacts with plagioclase to form anhydrite ($CaSO_4$) and H_2S needed
188 for sulfide mineralization. Other recent studies have invoked mechanisms such as the
189 destruction of previously sequestered metal-rich magmatic sulfides (Wilkinson 2013) or
190 anhydrite (Chambefort et al. 2008) in deeper or less evolved melts in order to address the
191 challenges of bringing together the required metals (via H_2O and Cl-bearing fluids) and
192 sulfur, to make a PCD.
193 Navigating the implications of MVP exsolution from Cu-rich melts, with or
194 without significant reduced or oxidized sulfur contents, and testing these new emerging
195 models for PCD formation requires that we place much tighter constraints on how ∑Cl,
196 fH_2S, fSO_2, and fO_2 might affect Cu-Mo partitioning. To examine the combined role of

chlorine and sulfur species in extracting and transporting Cu and Mo we will compare Cu/Mo partitioning in fluids containing only Cl-ligands to those with variable sulfur contents (fS_2), redox state (fO_2), and speciation (H_2S/SO_2). We have used emerging experimental techniques including CuAu-alloy tubing, in-situ quartz fracturing, metal-oxide fO_2 buffering and fluid inclusions (FI)-LA-ICPMS to characterize, quantitatively, reduced and oxidized Cu-Mo-S-Cl-bearing aqueous MVPs and silicate melts. With these data, and those from earlier experiments, we will then discuss the importance of these partitioning data for evaluating competing models of magmatic fluid evolution in arcs and PCD mineralization.

EXPERIMENT DESIGN

Our experiments were designed to simulate a synthetic, volatile-saturated magmatic system in which Cu and Mo equilibrate between a silicate melt and either a vapor-brine mixture (100 MPa) or a supercritical fluid (200 MPa). The experimental system allows for examining the relative affinity of Cu and Mo for MVPs at five different salinities (expressed as $\sum$Cl or X_{NaCleq} in the MVP)[3]. The experiments were run at reduced and oxidized conditions to allow for either H_2S or SO_2 to dominate the fluid's sulfur budget, enabling us to deconvolve the relative roles of redox and sulfur content on the Cl-dependent framework of previous experiments. Each experiment contained a quartz core to trap synthetic fluid inclusions for the purpose of tracking major and trace elements across all magmatic phases present in the experiments. Each experiment (100 or 200

[3] We use a corrected version of $NaCl_{eq}$ that treats 1 mole of $CaCl_2$ or $FeCl_2$ as 1.5 $NaCl_{eq}$ to account for the deviations in fluid salinity measurements and thus effective salinity of MVPs with significant Ca and Fe.

MPa) was allowed to equilibrate for 3 days at 725°C or 810 °C before using a thermal shock technique to fracture "in-situ" the quartz cores (Sterner and Bodnar 1991), and begin the process of trapping fluid inclusions. Given that the experiments needed to equilibrate in terms of fO_2, fS_2, as well as a_{Cu} and a_{Mo} in all phases, it was imperative to use in-situ fractured quartz to allow sufficient equilibration prior to fluid trapping (Tattitch et al. 2015). After 6 days, the run was "slow-quenched" over ~1 minute to prevent re-fracturing the quartz core while still cooling quickly enough to prevent diffusive re-equilibration of Cu and Mo in the melt during quench below the glass transition temperature (~ 500°C; Deubner et al. 2003). The quench glass and minerals provide for sampling the other magmatic phases. Smaller datasets of inclusion analyses were also obtained from inclusions trapped in the silicate glass in order to evaluate equilibrium.

Starting Materials

Experiments presented were run in custom-alloyed Cu_3Au_{97} capsules using the technique of Zajacz et al. (2011). The capsule material is permeable to H_2 allowing for control of fO_2 (Chou 1987); it is also resistant to reaction with sulfur species at all conditions, and serves to fix the a_{Cu} in the system ensuring quick equilibration of copper amongst the magmatic phases. The capsules were run inside Nimonic or Inconel alloy pressure vessels which buffer the fO_2 to 0.6±0.2 log units above the NNO[4] reference curve, based upon CoPd and NiPd fO_2-sensor capsule tests (Appendix I). More oxidized

[4] All experimental fO_2 values are referenced to log units above or below Ni-NiO buffer of O'Neill and Pownceby (1993) at the experimental P and T.

239 conditions were achieved by adding variable amounts of hematite to the water in the
240 pressure vessel, and thus overriding the so-called "intrinsic" fO_2 of the vessel. In the
241 oxidised runs CoPd and NiPd sensors indicate fO_2 ranged from NNO+1.8 to NNO+2.2 at
242 the end of the experiment. These values are below the magnetite-hematite buffer at run
243 conditions, reflecting that the rate of reaction of hematite to magnetite could not fully
244 consume all the H_2 generated by the vessel and the experiment despite hematite present at
245 the end of the runs. By running experiments at NNO+0.6 (intrinsic) and NNO+2 (added
246 hematite) we generated fluids dominated by H_2S or SO_2 respectively, whilst remaining
247 within a reasonable fO_2 range for arc magmas, and PCD in general.
248 Each experiment contained a felsic silicate melt at run conditions produced by
249 melting ground pumices from the rhyolitic Cardones Ignimbrite, Chile (Table 1; van
250 Zalinge et al. 2016). This material was chosen to simulate the evolved melts
251 representative of many ignimbrites throughout northern Chile that are chemically similar
252 to intrusive bodies associated with nearby PCD deposits. The melt composition fits
253 within the general compositional trend for other PCD partitioning experiments, that
254 utilize a melt close to the haplogranite minimum. Each experiment contained variable
255 amounts of natural molybdenite as well as chalcopyrite to maintain high levels of Mo and
256 Cu and promote accurate analyses. Crushed synthetic pyrrhotite, made at University of
257 Bristol, was added to all reduced experiments to promote sulfide equilibrium at the
258 desired fO_2/fS_2. Smaller amounts of chalcopyrite were added to oxidized runs to source
259 the sulfur, which was expected to oxidize to SO_2 and magnetite, yielding anhydrite
260 during the runs.

Each run contained one or two natural, fracture-free, inclusion-free quartz cores (2.6 mm OD) as a synthetic fluid inclusion trap. The silicate portion of each capsule was kept physically separate from the sulfide portion by placing the quartz core between them, and crimping the capsule around the quartz core (Figure 1). Longitudinal grooves were cut into the core to allow fluid to pass freely around it and facilitate equilibration of all magmatic phases. An aqueous solution containing NaCl, KCl, HCl, and 1000 ppm $CuCl_2$ was added with a micro-syringe to generate a vapor/brine- or supercritical MVP-bearing assemblage at run conditions. All starting material data are provided in Table 2.

MVP Compositions and Relevant Fugacities

The most critical aspect of these experiments is the controlled variation of the composition of the magmatic volatile assemblage, comprising either a single supercritical fluid or a coexisting vapor-brine mixture. The supercritical fluid produced in the 200 MPa experiments at 810 ^{o}C had a bulk salinity of ~12 wt% $NaCl_{eq}$ or a $\sum$Cl of 2.5 M. This is slightly higher than the upper end of the range that we would expect for fluids initially exsolved from an evolved, volatile-saturated arc magma (Audétat et al. 2008; Candela and Piccoli 2005). Running the same bulk composition at 810^{o}C and 100 MPa (below the critical point for NaCl-H_2O) results in the formation of coexisting low-salinity vapor and brine. A single "near-solidus" experiment was run at 725^{o}C and 100 MPa, which narrowed the expected salinity gap given the contraction of the two-phase field at these conditions (Bodnar et al. 1985; Driesner and Heinrich 2007). The salinities of the MVPs in each experiment were determined by microthermometry of the run product fluid inclusions, including corrections for additional colligative contributions of $CaCl_2$ and

284 $FeCl_2$. The experiments cover five different salinities (one supercritical, two exsolved
285 brine-vapour pairs) representative of the range of fluids that are generated from shallow
286 evolved magmatic intrusions, preserved in fluid inclusions (e.g. Audétat et al. 2008,
287 Beane and Bodnar 1995, Heinrich et al. 1999; Roedder 1971).

288 In addition to the chloride component of the fluids, each experiment contained a
289 significant amount of sulfur, which formed either H_2S or SO_2 at run conditions. Enough
290 chalcopyrite and pyrrhotite were added to the reduced experiment starting materials to
291 maintain sulfide saturation conditions for the melt and volatile phases. Equilibrium
292 between the chalcopyrite (average composition = 47 ± 0.5 mole% S), Cu-bearing
293 pyrrhotite (composition Fe =59 ± 0.2 wt%, S= 38 ± 0.3 wt%, Cu = 3 ± 0.1 wt%), MVPs
294 (log fO_2 = NNO+0.6), and magnetite all indicate reduced runs had an equilibrium log fS_2
295 ~ $1x10^{-3}$ MPa (Barton 1973; Mengason et al. 2010; Whitney 1984). Equilibrium between
296 S_2, H_2 and H_2O in the MVPs will then generate the dominant sulfur species in the
297 experiments, i.e. H_2S and SO_2. Using the program SUPCRIT92, and fugacity coefficients
298 from Churakov and Gottschalk (2003), we calculated the mole fraction of these species in
299 the MVPs at the reduced and oxidized conditions of the experiments. Reduced
300 experiments contain approximately 1.5 mol% H_2S in the vapor (X_{H2S} = 0.0149) with
301 negligible SO_2 (X_{SO2} = 0.00040). The much smaller amounts (~5mg) of chalcopyrite and
302 pyrrhotite added to the oxidized runs were completely destroyed[5], producing anhydrite
303 and magnetite, making sulfur available for the MVP and silicate melt. The total available

[5] Using sulfides to generate the necessary sulfur in the oxidized experiments is effective because although fS_2 at anhydrite saturation is higher than the reduced runs, it is below the level required for sulfide saturation at the more oxidized conditions; this is confirmed by the run-product assemblages.

sulfur and estimated anhydrite solubility (Newton and Manning 2005 and references therein) were used to estimate a $fS_2 = 2.5 \times 10^{-3}$ MPa; SUPCRIT92 calculations were then used to estimate the fSO_2 and fH_2S. The oxidized experiments are a near inversion of the ratio in the reduced experiments: 2.4 mol% SO_2 ($X_{SO2} = 0.024$) and much lower H_2S ($X_{H2S} \sim 0.003$). These values are comparable with those predicted by Whitney et al (1984) for sulfur-bearing magmatic gases in equilibrium with sulfides, as well as those for anhydrite saturation in saline aqueous fluids (Newton and Manning 2005). The range of experimental starting materials constrains the maximum ability of either H_2S or SO_2 to form complexes of Cu and Mo in fluids of almost any salinity. We will also draw upon results from published experimental data to extend these conditions beyond the $\sum$Cl and fS_2 range studied here.

ANALYTICAL METHODS

EPMA Analysis

Phase identification and major element quantification of the non-aqueous (silicate, sulfate and sulfide) experimental run products were made using a Cameca SX100 Electron Probe Microanalyzer. The solid run products were mounted in 1" epoxy rounds, polished and carbon-coated. Backscattered electron (BSE) images and Energy Dispersive Spectroscopy (EDS) were used for phase identification. Quantitative compositions for major elements (Na_2O, K_2O, CaO, FeO, MgO, MnO, TiO_2, Al_2O_3, SiO_2) and volatiles (S, Cl, H_2O) in run product glasses were determined using Wavelength Dispersive Spectrometry (WDS). An accelerating voltage of 15 kV, a beam current of 5 nA, and a beam diameter of 10 μm was used for all glass analyses. The low beam current used

minimizes diffusion of Na away from the analytical volume (Humphreys et al., 2006). Between 15 and 25 glass analyses were collected for each experiment, discarding some analyses for low totals (< 90%) and element ratios redolent of analytical overlap onto feldspar or quartz. Water contents were determined using the volatiles by-difference (VBD) method, assuming negligible CO_2, and cross-checked in two runs against the dissolved H_2O contents determined by SIMS.

Secondary Ion Mass Spectrometry (SIMS)

Dissolved H_2O and CO_2 in glasses from runs CMA201 and CMA224 were determined by SIMS using the Cameca ims1270 ion microprobe at University of Edinburgh with analytical conditions are described in detail in Mutch et al. (2016); Primary beam of $(O_2)^-$ ions accelerated to 12.2 kV and focussed to a ~15 μm diameter 4.2 nA beam at the sample surface (net impact energy of 22.2 kV). Positive secondary ions, with a 75±20 V offset to reduce molecular ion transmission, were acquired over a total of 10 analytical cycles (~10 minutes total analysis time). CO_2 (as ^{12}C) and H_2O (as ^{1}H) were analysed at high mass resolution ($M/\Delta M \approx 3000$) to resolve $^{12}C^+$ from $^{24}Mg^{2+}$. Calibration was carried out for background-corrected, ^{30}Si-normalised ^{1}H and ^{12}C ratios against a range of rhyolitic glass standards with ≤1.04 wt% CO_2 and ≤10 wt% H_2O. We additionally analysed for MgO (as $^{26}Mg^+$) and for CaO (as $^{44}Ca^{2+}$) using glass standards for calibration. These data provide more accurate values for glass MgO than EMPA at low concentrations (<0.1 wt%); for CaO the SIMS data provide a cross-check against EPMA. Eight glass spots were analysed from each run and the mean and s.d. concentration determined. Run CMA201 is homogeneous at the 12% relative level;

CMA224 shows some heterogeneity (25% relative). The glasses contained negligible CO_2 (≤10 ppm). H_2O contents agree within 0.5 wt% with VBD values for these two samples.

Fluid Inclusion Microthermometry

Microthermometric measurements were made on both vapor-brine and supercritical MVP experiments using a Linkam THMS600 and USGS microthermometry stages. The quartz core from each experiment was cut into several slices 300-1000 μm in thickness and doubly polished until a fluid inclusion assemblage of interest was within 50 μm of the surface. All supercritical inclusions (200 MPa), as well as vapor inclusions (100 MPa), were under-saturated in halite or sylvite at room temperature and their bulk salinity was determined by measuring the freezing point depression of water. Additional iterative corrections were made to the bulk salinity for the colligative effects of multi-chloride salts by treating the $CaCl_2$ and $FeCl_2$ components as contributing 1.5 $NaCl_{eq}$ per mole. Vapor-rich inclusions containing salt crystals (mixed inclusions) were discarded, as were any showing significant necking. Any individual inclusion with a freezing point temperature outside the 2σ standard deviation of the entire population of inclusions from the same experiment was also discarded as unrepresentative. Brine inclusions were identified at room temperature by the presence of both halite and sylvite daughter minerals and a smaller vapor bubble. Brine inclusion salinity was determined by measuring the combined sylvite and halite dissolution temperatures and then using the program SALTY (Bodnar et al. 1989). No brine inclusions were discarded on the basis of

372 microthermometric data, however deviation in Na/K ratio of the inclusions was used to
373 filter LA-ICPMS data for incomplete inclusion ablation.
374
375 *LA-ICPMS Analysis*
376 The major and trace element composition of run product fluid inclusions was
377 determined using laser ablation inductively coupled plasma mass spectrometry (LA-
378 ICPMS) at Virginia Tech using an Agilent 7500ce ICPMS and a GeoLas 193nm excimer
379 laser within a 1.8 cm^3 ablation cell. The quadrapole mass spectrometer allows for near-
380 simultaneous analysis of major (Na, K, Ca, Si, Al, Fe) and trace elements (Cu, Mo) down
381 to at least ppm levels (Heinrich et al. 2003; Gunther et al. 1998; Mutchler et al. 2008).
382 Unfortunately, the O_2 mass interferences for S did not allow us to quantify the S content
383 of the fluid inclusions. Inclusions with no evidence of necking and without neighbouring
384 inclusions within the analytical volume were selected for analysis. An energy density of
385 ~10 J/cm^2 and a pulse rate of 5 Hz was used to ablate through the overlying quartz host
386 and into the individual inclusions while stepwise increasing the spot size from 10-16 μm
387 up to just larger than the inclusion diameter. Each signal was then integrated and
388 concentrations determined using the salinity as the internal standard. Results from
389 microthermometry were used to determine salinity, which was then used to calculate the
390 ∑Cl to balance the Na, K and Ca present in the inclusions. Roughly 30% of the inclusions
391 ablated were not usable as the quartz fractured or the inclusion was positioned too deep
392 for detection of all elements. A small number of inclusions were discarded based on large
393 deviations in their Na/K ratios (>2σ) from those determined by microthermometry. A

fluid inclusion assemblage was then defined by the average of all the inclusions of a single type (vapor, brine, supercritical) for each experiment.

Run product silicate glasses were also analysed for Cu and Mo by LA-ICPMS. A lower energy density of ~7 J/cm^2 was used along with 60 μm spot size to homogenize the analyses. Analyses of 6-10 individual spots were standardized against Na from EMPA analyses and averaged to yield Cu and Mo concentrations for each synthetic melt.

RESULTS

Experimental Run Products

Each experiment produced a quenched glass containing a magmatic mineral assemblage. The 200 MPa experiments had much higher melt fractions owing to the higher water solubility and lower liquidus temperature (Fig 2A-B). The reduced experiments (CMA406 and CMA407) contained abundant chalcopyrite and molybdenite along with clinopyroxene and minor amounts of apatite and plagioclase (Fig 2A). There is little evidence for any micron or sub-micron sulfide grains in the glasses that would hinder trace element analyses. Gold nuggets and small sulfides are observed in some glass analyses and on occasion clearly impact an otherwise stable Cu signal; these periods of ablation were not used to quantify any trace elements.

The oxidized experiments (CMA420 and CMA421) contain abundant anhydrite, often found inside holes formed by volatile bubbles in the glass (Fig 2B and 2D), with no observable remaining chalcopyrite. These experiments lack any Ca-rich silicates (clinopyroxene, plagioclase) and contain instead Ca-poor amphibole and biotite (Fig 2B). However, the experiments remain saturated in molybdenite, owing to its stability at lower

417 a_{H2S} than Cu-Fe sulfides under oxidizing conditions (Audétat et al. 2011). The 100MPa
418 experiments show the same exchange of sulfides (CMA201) for sulfates (CMA224) with
419 increased oxidation. However, as the melt fraction is lower, these experiments also have
420 more abundant amphibole, biotite, and plagioclase or anhydrite with minor amounts of K-
421 feldspar (Fig 2C-D) in addition to relict plagioclase and quartz from the starting material.
422 The near-solidus experiment (CMA303) contained only a small amount of quench glass
423 due to a much higher overall crystallinity, yet has the same mineral assemblage as the
424 higher temperature runs.
425 In addition to glass, every experiment contained larger mineral run product
426 minerals including: the starting sulfides, newly formed magnetite, and overgrown quartz
427 cores with fluid inclusions. The quartz cores contained assemblages of fluid inclusions
428 (supercritical at 200 MPa, coexisting vapor and brine at 100 MPa) contained within the
429 regrown or "healed" fractures. The composition of larger pieces of run product sulfides
430 were used to confirm the fS_2 in the reduced experiments using the Cu-adjusted algorithm
431 of Mengason et al (2010).
432
433 *Silicate Melt Composition*
434 The major element compositions of the run product glasses are shown in Table 3.
435 The more oxidized experiments have melts that show significant depletion of CaO due to
436 the crystallization of anhydrite. As a result, the oxidized experiments have an aluminium
437 saturation index (ASI) that is more peraluminous (ASI = 1.04 to 1.19) compared to the
438 generally close to metaluminous glasses from reduced runs (ASI = 1.02-1.05). The sulfur
439 content of the oxidized runs is also elevated (~200 ppm S) compared to the reduced runs

(~90 ppm S) owing to the higher solubility of S^{6+} compared to S^{2-} (Clemente et al. 2004; Zajacz 2015). Interestingly, the Cl content of the melt also varies; the oxidized runs have a slightly lower Cl despite the same ∑Cl in the experiments. This is likely due to the change in melt aluminosity resulting from CaO loss to anhydrite crystallization. Water contents of the melt vary from 4.4 to 6.9 (Table 3). EMPA by-difference values are higher than SIMS, but agree at the 1 s.d. level.

The Cu and Mo concentrations of each experiment are also reported in Table 3. Experiment CMA406 contains less Cu than the other supercritical run due to using a lower a_{Cu} capsule (Cu_2Au_{97}). This was to ensure that any apparent deviation in Cu partitioning was not dependant on the a_{Cu} used for a given experiment. All melts remained saturated in molybdenite and thus any variability in melt Mo content must be the result of variability in solubility as a function of composition, P, T or fO_2. The Mo concentration of the melt from the oxidized runs (43-59 ppm) is consistently 2-5 times greater than those from the reduced runs (10-28 ppm). This trend with oxidation is in good agreement with recent experimental data quantifying the solubility of molybdenite in granitic melts of similar composition to ours (Sun et al. 2014).

Fluid Inclusion Types and Compositions

We characterized assemblages of fluid inclusions from each experiment, which trapped samples of either a single supercritical fluid or coexisting vapor and brine at magmatic conditions. The relative size of the contraction vapor bubble decreases with increasing MVP salinity and density, and halite and sylvite are observed in the brine inclusions from all subcritical, 100 MPa runs (Fig 3). Inclusions trapping MVPs from

463 reduced experiments always contained one or more small opaque daughter minerals
464 inferred to be (Cu)-Fe sulfides (chalcopyrite or pyrrhotite) and molybdenite (Fig 3 A-E)
465 precipitated from the fluids on quench. Fluid inclusions trapped in the more oxidized runs
466 occasionally contain dark daughter minerals inferred to be molybdenite (Fig 3 I-L) and
467 occasionally translucent, red daughter minerals that may be K-Fe-Cl phases observed in
468 other fluid inclusion studies (e.g. Anthony et al. 1984; Kodera et al. 2003). The oxidized
469 fluid inclusions also often contained minor transparent daughter minerals that did not
470 melt upon heating to 550 ^{o}C, well above the otherwise common salt disappearance
471 temperatures, indicating that they are neither halite nor sylvite (Fig 3 F, I, K, L). We have
472 inferred that these are an unidentified sulfate phase(s) formed due to the high SO_2 content
473 of the oxidized MVPs.
474 The fluid inclusion LA-ICPMS data show a strong increase in the Cu
475 concentration of higher salinity supercritical and brine MVPs compared to the lower
476 salinity vapors. Reduced experiments containing abundant H_2S have elevated Cu
477 concentrations in all MVP phases compared to those from the oxidized, SO_2-dominated
478 runs. Trends for Mo are not as readily apparent from the raw data but an increase in Mo
479 concentration function of salinity is still apparent.
480
481 *Partition Coefficients*
482 There is ubiquitous evidence that primary supercritical fluids exsolved from their
483 parent melt undergo phase separation into coexisting brine and vapor, which persist down
484 to sub-solidus/ore zone conditions where fluid-melt partition coefficients are no longer
485 relevant. Thus, it is critical to understand both fluid-melt and brine-vapor partitioning to

understand the evolution of proto-ore fluids. For each experiment we report the partition coefficient for each of the MVPs (vapor, brine, and supercritical) relative to the silicate melt (Table 5) and brine-vapor partition coefficients for 100 MPa runs. Replicate experiments show averaged values that deviate by less than 1 sigma, indicating that the principle source of the reported uncertainty is analytical in origin. As a result, we have a high degree of confidence that these data are representative of ore metal partitioning behaviour over the P-T-fO_2 range examined. In addition, fluid inclusions sampling the supercritical MVPs at 200 MPa and brines at 100 MPa from the quartz-hosted assemblages have been compared to a smaller set of inclusions hosted in the glass from each of the runs (excluding CMA406) to evaluate equilibrium between the time of quartz trapping and the quench. (Appendix II). Plotting their relative Cu and Mo contents (Fig 7 – Appendix II) shows clearly that the inclusions in both hosts are a good match to each other and thus strongly suggests that both the quartz-hosted inclusions and silicate glass represent sampling of equilibrium magmatic phases. However, due to significant concentrations of most of the major elements (Na, K, Ca, Fe) in the host glass, some or all of these elements are often not resolvable in the LA-ICPMS data for the glass-hosted inclusions. In addition, more inclusions were discarded due to no resolvable major element signal. Given their incomplete characterization and limited dataset, none of the glass-hosted inclusions have been included in the averages reported below.

Major Element Partitioning (Cl, Fe, S)

Given the expectation of a strong influence of Cl, the fluid melt partition coefficients are given along with their respective ∑Cl as both X_{NaCleq} and wt% salinity for

509 convenience. The initial Cl added to the starting materials and the NaCl-H_2O solvus for
510 the P-T conditions controls these values for each experiment. The apparent $D_{Cl}^{f/m}$ between
511 vapor and melt or fluid and melt is also shown in Table 5 and varies from12 (±4) at
512 X_{NaCleq} = 0.01 (~3wt%), 25 (±5) at X_{NaCleq} = 0.016 (5wt%) at 100 MPa, to either 33 (±4)
513 or 44 (±6) at X_{NaCleq} = 0.044 (13wt%) at 200 MPa. The variability in these D_{Cl} values
514 will be discussed below as a function of the ∑Cl in the fluid, pressure, and changes to
515 melt composition.

516 The importance of Fe in the formation of PCD cannot be overstated, with Fe-S
517 minerals representing the bulk of the ore and the most significant elemental anomalies
518 that define a PCD. To explore the role of Fe we also report the $D_{Fe}^{f/m}$ and $D_{Fe}^{b/v}$ for relevant
519 experiments. For the evolved melts used in this study Fe partitioning increases strongly as
520 a function of salinity. The measured $D_{Fe}^{f/m}$ increases from 0.6 (±0.2) for vapor at X_{NaCleq} =
521 0.01, to 2.1 (±0.5) for supercritical fluids at X_{NaCleq} = 0.044. Given that Fe is a significant
522 component of silicate melts, the absolute value of $D_{Fe}^{f/m}$ may vary with a_{FeO} in the silicate
523 melt. The brine-melt partition coefficient ($D_{Fe}^{b/m}$) = 12 (±4) and the brine-vapor partition
524 coefficient ($D_{Fe}^{b/v}$) = 23 (±12). The presence of reduced sulfur and increased Fe^{2+} does
525 increase Fe partition coefficients, and our reduced, S-bearing experiments have $D_{Fe}^{f/m}$
526 values of 0.77 (±0.38), 3.3 (±1.2), and 30 (±10) for vapors, supercritical fluids and brines
527 respectively.

528 Although our experiments do not measure S directly we can infer $D_S^{f/m}$ values of
529 ~ 200 for reduced and oxidized conditions based on the calculated values of ~2 or ~4
530 wt% S in the MVPs and measured values of ~100 or ~200 ppm S in the melt (Table 3) at

reduced and oxidized conditions respectively. This is of the same magnitude reported by Webster et al. (2011) of ~50 < $D_S^{f/m}$ < ~200 at 900 °C, 200MPa and similar fO_2 values (NNO-0.4 to NNO+1.4), Massotta et al. (2016) for rhyolite at 200 MPa and Re-ReO_2 buffered fO_2 ($D_S^{f/m}$= 101±19 at 900 °C and 114±43 at 800 °C), as well as results from Zajacz et al. (2015) for "rhyolite like melts" at higher pressure and temperature ($D_S^{f/m}$ =200 at 500 MPa and ~1250 °C).

Copper Partitioning

We report fluid/melt and brine/vapor (100 MPa) partition coefficients for Cu as a function of the X_{NaCleq} (salinity) and X_{H2S}/X_{SO2} (Table 5). In the oxidized experiments (NNO + 2) we observe much stronger partitioning of Cu into supercritical fluids of moderate salinity compared to a lower salinity vapor (oxidized $D_{Cu}^{s/m}$= 140 ± 25 at X_{NaCleq} = 0.044 (13wt%) compared to $D_{Cu}^{v/m}$ =18 ± 9 at X_{NaCleq} = 0.016 (5wt%) and $D_{Cu}^{v/m}$= 9 ± 5 at X_{NaCleq} = 0.01 (~3wt%)). However, partitioning of Cu into magmatic brine appears to maintain the same strong enrichment in Cu as for supercritical fluids (oxidized $D_{Cu}^{b/m}$ = 165 ± 90). Given that brines may separate from a single fluid phase as it decompresses at sub-solidus temperatures, we also note the partitioning of Cu between the vapor and brine and, here again, we observe a marked salinity dependence. The $D_{Cu}^{b/v}$ increases by a factor two, from 9 ± 5 to 19 ± 11, as the ratio of Cl in the brine over the vapor ($\sum Cl^{b/v}$) increases from 10 to 20. Experiments at reduced conditions (NNO + 0.6) show the same trends albeit with somewhat increased partitioning from melt into MVPs; $D_{Cu}^{v/m}$= 40 ± 9 increases to $D_{Cu}^{s/m}$= 280 ± 78 as we increase the salinity from X_{NaCleq} = 0.01 (~3wt%) to X_{NaCleq} =

553 0.044 (13wt%). The brine maintains the strong Cl-dependent partitioning observed for
554 supercritical fluids (reduced $D_{Cu}^{b/m} = 310 \pm 100$). While the brine still dominates the vapor
555 in terms of Cu content, the $D_{Cu}^{b/v}$ decreases to 10 ± 4 at a $\sum Cl^{b/v}$ ratio of 20 due to Cu
556 concentration in the vapor increasing in the presence of reduced sulfur ligands more
557 strongly than it does in the brine.
558
559 *Molybdenum Partitioning*
560 Partitioning data for Mo also show a consistent preference of Mo for the MVPs
561 relative to the silicate melt. The reduced experiments show an overall lower affinity of
562 Mo for the MVPs increasing from $D_{Mo}^{v/m} = 2.0 \pm 0.8$ at $X_{NaCleq} = 0.01$ (~3wt%) through
563 $D_{Mo}^{s/m} = 7.8 \pm 1.8$ at $X_{NaCleq} = 0.044$ (13wt%) for intermediate supercritical fluids, up to
564 $D_{Cu}^{b/m} = 71 \pm 22$ at $X_{NaCleq} = 0.33$ (62wt%) for magmatic brine. The oxidized experiments
565 sample a larger salinity range but the same trend is observed with slightly elevated
566 partitioning into MVPs over the silicate melt relative to reduced experiments ($D_{Mo}^{v/m}$
567 increases from 4.3 ± 2.2 at $X_{NaCleq} = 0.01$ (~3wt%), to 6.9 ± 3.6 at $X_{NaCleq} = 0.016$ (5wt%)
568 through $D_{Mo}^{s/m} = 21 \pm 5$ at $X_{NaCleq} = 0.044$ (13wt%) up to $D_{Mo}^{b/m} = 130 \pm 10$ for oxidized
569 magmatic brines (53wt% and 62wt%).

570 **DISCUSSION**

571 *Magmatic Cu Partitioning*
572 A fundamental step in modelling Cu extraction from magmas by MVPs is
573 identifying the critical fluid parameters (X_{NaCleq}) and ligands that control Cu partitioning
574 and transport. Despite a suite of experimental studies that highlight the dominance of Cl

575 in controlling this partitioning (Candela and Holland 1984; Frank et al. 2011; Simon et al.
576 2006; Tattitch et al. 2015; Zajacz et al. 2011), there remain contrary claims based on both
577 natural and synthetic systems. As previously noted, the complications of Cu diffusion in
578 natural systems require that we exercise caution when interpreting data from quartz-
579 hosted fluid inclusions in natural systems, especially those experiencing repeated fluid-
580 fluxing events (Lerchbaumer and Audétat 2012; Seo and Heinrich 2013). These studies
581 highlight that even well-sealed vapor inclusions can readjust their Cu concentrations via
582 diffusion. In addition Seo and Heinrich (2013) provide some of the first topaz-hosted Cu
583 partitioning data which accord perfectly with our experimental trends (see Section 5.1).
584 There are very few experimental studies that make claims of Cu partitioning into
585 vapor relative to coexisting brines, that would refute the dominance of Cl in controlling
586 Cu partitioning. A well-known example is the study by Nagaseki and Hayashi (2008) that
587 purports to show magmatic vapor with Cu concentrations greater than coexisting brine at
588 (500-650 ^{o}C). However, their data rely upon the analysis of less than 5 vapor inclusions
589 per run, with generally only 1 to 3 analyses reported. We are wary of fluid inclusion
590 analyses where only a few individual inclusions are measured as the chances of
591 unrepresentative analyses are high; likewise, population averages with 1σ uncertainties
592 greater than 50% remain highly suspect. Moreover, duplication of one of the Nagaseki
593 and Hayashi (2008) runs by Lerchbaumer and Audétat (2012) disagrees with the original
594 experiments, yielding instead results consistent with brine-dominated Cu partitioning.
595 Thus the data of Nagaseki and Hayashi (2008) are in conflict with those presented herein,
596 existing magmatic copper partitioning data (Frank et al. 2011; Lerchbaumner and Audétat
597 2012; Simon et al. 2006; Zajacz et al. 2011) as well as work of Pokrovski et al. (2008) for

598 hydrothermal fluids at similar conditions (350 ^{o}C and 500 ^{o}C). These studies highlight
599 that, while sulfur will increase Cu concentration in vapors relative to brines, even ~1 wt%
600 S does not result in a preference of Cu for the vapor phase. As a result we will discuss
601 how the bulk of the existing magmatic Cu partitioning data can be combined with our
602 new data to provide a more comprehensive picture of Cu extraction and transport.
603
604 *Magmatic Cu Partitioning into MVPs as a Function of ∑Cl*
605 Compilation of our new Cu partitioning data along with existing literature data
606 over broad range of X_{NaCleq}, P, T and fO_2/fS_2 conditions relevant to MVP exsolution
607 from silica-rich arc magmas (Fig 4) shows a strong (and quantifiable) relationship
608 between Cu partitioning and salinity (X_{NaCleq}). Several prior studies of Cu partitioning
609 that also show the relationship between Cu and Cl have been excluded due to limitations
610 of their experiment designs. Candela and Holland (1984), Keppler and Wylie (1991) and
611 Williams et al. (1997) all show a strong correlation between Cu and Cl, but rely on
612 quenched fluids to characterize Cu concentrations. It is our belief that this method does
613 not quantitatively retain the metal-chloride complexes unique to the high-temperature
614 MVPs responsible for extraction and early transport of Cu and Mo (see below). Thus,
615 while they do highlight the importance of Cl, they have not been included in the
616 empirical fitting of Cu partitioning data described below.
617 The included data show that Cu will partition into supercritical fluids of modest
618 salinity (X_{NaCleq} = 0.015 to 0.044 or ~ 5 to 13 wt% $NaCl_{eq}$) at concentrations ~50 to more
619 than 300 times greater than the silicate melt from which they exsolve. The extraction of
620 Cu into MVPs of lower salinity will decrease sharply (Fig 4 - green line) with very

621 inefficient extraction below ~3wt% $NaCl_{eq}$ to a point where Cu will become compatible
622 in the silicate melt relative to MVPs at salinities below ~1wt% $NaCl_{eq}$. Such low salinity
623 (< 3wt%) MVPs are therefore incapable of sequestering and concentrating Cu from
624 silicate melts in the pressure range studied.

625 Whereas most arc magmas are unlikely to attain brine saturation prior to reaching
626 the solidus (Audétat et al. 2008), the formation of brines in the sub-solidus magmatic
627 environment, or in the fluid fluxing pathways above the magmatic hearth, will exert a
628 strong control on the fate of Cu previously extracted from the magma by single-phase
629 fluids. As a primary, Cu-rich, MVP decompresses, it will intersect the NaCl-H_2O solvus
630 and undergo phase separation. Our examination of Cu partitioning shows that when
631 supercritical fluids undergo phase separation the near-magmatic (or "tardo-magmatic")
632 brines always have an increased capacity to sequester the available Cu compared to the
633 coexisting vapor (Fig 4). As the solvus expands with deceasing pressure, the ability of the
634 brine to concentrate Cu increases, as the salinity and Cu content of the coexisting vapor
635 will continually decrease as pressure drops.

636 The combined suite of partitioning data also provides information on Cu
637 complexation mechanisms in MVPs. At very low concentrations of ∑Cl (Figure 4) the
638 experimental data suggest that a simple Cu-Cl complexation mechanism operates. The
639 logarithmic slope of ~1 for X_{NaCleq} values below ~ 0.005 (~2 wt% $NaCl_{eq}$) indicates a 1:1
640 Cu:Cl ratio, suggestive of complexation according to the equilibrium:

641 $$CuO_{0.5}^{melt} + NaCl^{MVP} = (CuCl^0)^{MVP} + NaO_{0.5}^{MVP} \quad (1)$$

642 Thus at very low ∑Cl there may be insufficent Cl to form larger ion pair complexes but a
643 narrow range where $CuCl^0$ may become important. However, Cu is already only slightly

644 favoured in the MVPs at this point, and as the X_{NaCleq} continues to decrease below 0.002,
645 Cu will become compatible in evolved melts due to minimal solubility of Cu in an MVP
646 lacking adequate ∑Cl. The quench experiments by Candela and Holland (1984) explore
647 Cu partitioning into supercritical fluids within this very low salinity range, and can be
648 used to help pin down the intercept of $D_{Cu}^{f/m}$ at $X_{NaCleq} = 0$ ($D_{Cu^0}^{f/m}$=0.8 ± 0.5).

649 The logarithmic relationship between Cu and ∑Cl in the combined suite of
650 experiments presented over the salinity range 2 wt% to 13 wt% has a slope of ~2 (Figure
651 4), indicating a 1:2 ratio for Cu:Cl. This is consistent with the bent-linear
652 $(Na,K)^+\{CuCl_2\}^-$ associated ion pair complex predicted by Zajacz et al. (2011) and
653 supported by numerous other studies of magmatic Cu partitioning (Frank et al. 2011;
654 Simon et al. 2006; Tattitch et al. 2015). For these primary, saline, magmatic MVPs, the
655 experimental data support the proposition that Cu complexation is dominantly controlled
656 by $(Na,K)CuCl_2$ as follows:

657 $$CuO_{0.5}^{melt} + 2NaCl^{MVP} = Na^+\{CuCl_2\}^- + NaO_{0.5}^{MVP} \quad (2)$$

658 Analogous equilibria can be written to describe the exchange of Cu with KCl and HCl in
659 the MVPs. Thermodynamic calculations presented by Zajacz et al. (2011) indicate that
660 the K^+ version of the Cu complex in equation 1 is slightly favoured over the Na^+ version,
661 but that both are far more stable than the H^+ version. As a result, MVPs exsolved from
662 strongly peraluminous systems with a high H:Na-K ratio in the MVPs (e.g. Williams et
663 al. 1997) may have a more limited capacity for extraction of Cu.

664 We can combine this lower stability for $CuCl^0$ with the much more pronounced
665 $(Na,K)CuCl_2$ complexation mechanism to form a quantitative model for Cu extraction by
666 first combining the equilibrium constants (K_{EQ1} and K_{EQ2}) for equations (1) and (2);

667 $$K_{EQ2} = \frac{a\left(NaCuCl_2\right) \cdot a\left(NaO_{0.5}^{melt}\right)}{\left(X_{NaCl}\right)^2 \cdot a\left(CuO_{0.5}^{melt}\right)} \quad (3)$$

668 $$K_{EQ1} = \frac{a\left(CuCl^0\right) \cdot a\left(NaO_{0.5}^{melt}\right)}{\left(X_{NaCl}\right) \cdot a\left(CuO_{0.5}^{melt}\right)} \quad (4)$$

669 (along with analogous equations for K) and then rearranging the equation to define Cu
670 partitioning as a function of NaCl/KCl and the equilibrium constants K_{EQ1} and K_{EQ2}:

671 $$D_{Cu}^{f/m} = \frac{a\left(NaCuCl_2\right) + a\left(KCuCl_2\right) + a\left(CuCl^0\right)}{a\left(CuO_{0.5}^{melt}\right)} = \frac{K_{EQ2} \cdot \left(X_{NaCl}\right)^2 + K_{EQ1} \cdot \left(X_{NaCl}\right)}{a\left(NaO_{0.5}^{melt}\right)} + \frac{K_{EQ2b} \cdot \left(X_{KCl}\right)^2 + K_{EQ1b} \cdot \left(X_{KCl}\right)}{a\left(KO_{0.5}^{melt}\right)} \quad (5)$$

672 Given that Zajacz et al. (2011) predict that K_{NaCl}:K_{KCl} ratio is close to unity we will
673 assume that variability in fluid NaCl:KCl, (or magmatic Na_2O:K_2O) ratios will have
674 negligible effects on partitioning, thus we adopt $NaCl_{eq}$ as a definition of salinity. The
675 stability of $HCuCl_2$ complexes is predicted to be lower than Na-K complexation,
676 however, we have not resolved the effect of variable HCl on the $D_{Cu}^{f/m}$.

677 "Intermediate" salinity fluids (5wt% to 40 wt%) show a strong excess capacity to
678 extract Cu from the melt above that soluble as simple $CuCl^0$ species (Figure 4). By
679 simplifying Eq 5 assuming that (i) $NaCuCl_2$ and $KCuCl_2$ behave similarly; (ii) $CuCl^0$
680 dominates the fluid at low salinity; and (iii) fitting the Cl-free $D_{Cu}^{f/m}$ by adding in the
681 lowest salinity point from Candela and Holland (1984) we obtain an expression to predict
682 copper partitioning as a function of X_{NaCleq} in the MVP for melts of similar Na/K and
683 ASI:

684 $$D_{Cu}^{f/m} = K_2\left(X_{NaCleq}\right)^2 + K_1\left(X_{NaCleq}\right) + D_{Cu^0}^{f/m} \quad (6)$$

This functional form ignores the changes to the MVP as we transition from a supercritical fluid towards high-salinity brine and ultimately a wet salt melt. The excess Cu capacity of the intermediate MVPs is contingent on the stability of the (Na,K)$CuCl_2$ complex; which is in turn contingent on the partial dissociation of NaCl and/or solvation in fluid.

As an exsolved Cl-rich MVP transitions from an intermediate salinity supercritical fluid towards phase separation, the stability of the dominant (Na,K)$CuCl_2$ complex appears to decrease, as manifest in the decline in $D_{Cu}^{f/m}$ as X_{NaCleq} increases above 0.1 (Figure 4). At still higher X_{NaCleq} the partitioning trend returns to that for $CuCl^0$ (Figure 4 dashed line) consistent with a transition of the MVP towards an NaCl-KCl "wet salt melt" with low H_2O activity (or X_{H2O}), eventually converging on pure NaCl (X_{NaCleq} =1). Under these conditions the alkali-chloride component of the MVP remains increasingly associated and the dominant Cu complexation moves back towards a $CuCl^0$ component. In effect, decreasing X_{H2O} limits the stability of (Na,K)$CuCl_2$, which implies in turn that this complex is solvated significantly by H_2O. We can capture this change by including a solvation parameter for (Na,K)$CuCl_2$ in the partitioning equation as follows:

$$D_{Cu}^{f/m} = K_2\left[\left(X_{NaCleq}\right)^2 * \left(X_{H_2O}\right)^Z\right] + K_1\left(X_{NaCleq}\right) + D_{Cu^0}^{f/m} \quad (7)$$

where Z represents an unknown number of H_2O species associated with the (Na,K)$CuCl_2$ complex. We can then fit this equation to the combined dataset using a weighted least squares regression to obtain the final expression for $D_{Cu}^{f/m}$ as a function of X_{NaCleq} and X_{H2O} for MVPs of any salinity:

$$D_{Cu}^{f/m} = 8.0x10^4(\pm 1.4x10^4)\left[\left(X_{NaCleq}\right)^2 * \left(X_{H_2O}\right)^{14\pm 2}\right] + 380(\pm 50)\left(X_{NaCleq}\right) + 0.8(\pm 0.5) \quad (8)$$

706 This expression provides a robust fit to all of the experimental data across all the
707 experiment designs (R^2=0.94 and <25% relative uncertainty on K's) with the exception of
708 one datum from Frank et al. (2011), which shows anomalously low $D_{Cu}^{f/m}$. In addition, we
709 see further evidence that while the data from Candela and Holland (1984) highlight the
710 control of Cl on Cu partitioning, the quenched fluids follow the estimated line for $CuCl^0$
711 only (Fig. 4 – black crosses) and do not record the additional Cu extraction capacity of
712 MVPs due to (Na,K)$CuCl_2$ complexation. Using Equation (8), we can model $D_{Cu}^{f/m}$ over
713 any salinity range, with a particularly high density of experiments covering the range of
714 salinities expected for initial exsolution of a magmatic supercritical fluid (roughly 0 to 12
715 wt% $NaCl_{eq}$). Although variations in Na/K/H likely affect partitioning, the combined
716 dataset covers metaluminous (ASI~1) to peraluminous (ASI~1.2) melt compositions
717 relevant to PCD formation. In addition, the impacts of other common salts (e.g. $CaCl_2$
718 and $FeCl_2$) on $D_{Cu}^{f/m}$ at high temperature are poorly constrained. Thus, the data presented,
719 and empirical fit for $D_{Cu}^{f/m}$ as a function of X_{NaCleq}, are appropriate for MVPs where NaCl
720 and KCl dominate the chloride budget. Particulary HCl-rich systems, or those dominated
721 by other salts, would require additional parameterization to accurately predict Cu
722 partitioning.

723 The trend for Cu partitioning between coexisting brine and vapor (Figure 5) is
724 much simpler than that for Cu partitioning between fluid and melt (c.f. Figure 4). As the
725 ratio of ∑Cl in the brine to that in the vapor increases during decompression ($D_{Cl}^{b/v}$
726 increases from ~1 to ~100) so the capacity of the vapor to carry Cu will fall and that of
727 the brine will increase in proportion to $D_{Cl}^{b/v}$. The well-established NaCl-H_2O solvus and

728 the combined dataset presented in Fig 5 highlight that magmatic fluids ascending to
729 shallow levels (<75 MPa) will inevitably phase separate, forming Cu-rich brines during
730 decompression, that will sequestering the majority of the original Cl and Cu. These
731 metal-rich "brine reservoirs" can accumulate and remain stable in the sub-solidus host
732 rocks for ≥30,000 years above the parental melt, as shown by the numerical models of
733 Weis (2015). Coexisting phase compositions for brines and vapors suggested by
734 numerous studies of PCD (e.g. Audétat et al. 2008; Heinrich 2005; Heinrich et al. 1999;
735 Rusk et al. 2008) indicate that brine-saturated vapors with ≤1-3 wt% $NaCl_{eq}$ coexist with
736 smaller amounts of very saline brine (~30wt% to >60wt% $NaCl_{eq}$) due to phase
737 separation of an originally supercritical fluid opon decompression to pressures between
738 90 to <50 MPa. The bulk H_2O:Cl ratio of low-pressure (~100 MPa) melt inclusions in
739 silicic volcanic rocks (e.g. Blundy et al. 2008) and fluid inclusions measured in PCD (e.g.
740 Audétat et al. 2008; Heinrich et al. 1999) suggest that supercritical fluid input salinity
741 ranges from ~5wt% to 8wt% $NaCl_{eq}$ are common (e.g. Candela and Piccoli 2005;
742 Lerchbaumer and Audétat 2012). Given these values and the Cu partitioning we report, at
743 least 50% to >85% of the *total mass fraction* of Cu available for mineralization will be
744 sequestered into the volumetrically minor brine phases during fluid ascent and unmixing,
745 consistent with observations of other recent studies that utilize experimental data for Cu
746 partitioning (e.g. Lerchbaumer and Audétat 2012). This does not account for any Cu lost
747 from escaping vapor due to sub-lithostatic venting (likely associated with brecciation)
748 that would cause additional brine separation. In both cases the accumulated brine
749 phase(s) will become more enriched in Cu and dominate the Cu mineralization potential
750 of the system. In some cases evidence exists for mineralized veins formed directly from

751 metal-rich brine with no role of a previously separated low-density vapor (e.g. Wilson et
752 al. 2003). As a result, the fate of brines, the details of their role in pervasive potassic
753 alteration, and the mechanism by which their Cu content can become mineralized as
754 sulfides, plays a critical role in PCD formation.
755
756 *The Influence of fO_2 and fS_2 on MVP Cu Partitioning*
757 The dominant control on Cu partitioning and transport into MVPs is demonstrably
758 their Cl content. However, our Cu partitioning data, along with those of other
759 experimental studies (e.g. Frank et al. 2011, Simon et al. 2006, Zajacz et al. 2011),
760 indicate that the presence of reduced sulfur species can enhance the amount of Cu that
761 partitions into magmatic MVPs, especially in magmatic vapor relative to coexisting brine
762 (Fig 4 and 5 yellow symbols). This is likely due to the stability of a modified version of
763 the (Na,K)$CuCl_2$ binary ligand complex where HS^- replaces one of the Cl^- ligands (Mei et
764 al. 2013; Zajacz et al. 2011):
765 $$Na^+\{CuCl_2\}^- + H_2S^{MVP} = Na^+\{CuCl(HS)\}^- + HCl^{MVP} \quad (9)$$
766 This complex forms under reduced conditions where H_2S or HS^- dominate the sulfur
767 budget of the lower density MVPs. It is also clear from Figures 4 and 5 that the ability of
768 H_2S to influence Cu complexation and extraction is subordinate to that of Cl, and under
769 none of the experimental conditions discussed (350 to 810 ^oC at ~40 MPa to 200 MPa)
770 does the magmatic vapor show a stronger affinity for Cu than a coexisting brine (Fig 5 -
771 yellow filled symbols). We can parameterize the impact of H_2S on $D_{Cu}^{f/m}$ using the
772 equilibrium between the previously defined $NaCuCl_2$ complex from low-H_2S systems and
773 NaCuClHS (Eq 9):

774
$$D_{Cu}^{f/m} * [CuO]_{melt} = [NaCuCl_2] + [NaCuClHS] + [CuCl^0] + [NaCuHS_2] + [Cu]$$
$$[NaCuClHS] = K_1\left[\left(X_{NaCleq}\right)^2 * \left(X_{H_2O}\right)^Z\right] * K_9 * X_{H_2S} * \left(X_{H_2O}\right)^Y \quad (10)$$

775 which simplifies to:

776
$$D_{Cu}^{f/m} = K_1\left[\left(X_{NaCleq}\right)^2 * \left\{\left(X_{H_2O}\right)^Z + K_9\left(X_{H_2S}\right)\left(X_{H_2O}\right)^Y\right\}\right] + K_2\left(X_{NaCleq}\right) + [NaCuHS_2] \quad (11)$$

777 Where the Y and Z terms represent the hydration parameters for the NaCuClHS and
778 $NaClCl_2$ complexes respectively, and K_1, K_2, and K_9 are the equilibrium constants for the
779 equations described above.

780 The *ab initio* thermodynamic calculations, backed by fluid solubility data for Cu,
781 presented by Zajacz et al. (2011), also show that HS^- alone cannot stabilize significant
782 quantities of Cu in an MVP; Cl and alkali cations are required. This is due to the limited
783 stability of the binary $(Na,K,H)^+Cu(HS)_2^-$ complexes formed via the equilibrium:

784
$$CuO_{0.5}^{melt} + 2H_2S^{MVP} = Na^+\{Cu(HS)_2\}^- + H_2 \quad (12)$$

785 Zajacz et al's (2011) calculations are supported by the strong dependence of our reported
786 $D_{Cu}^{f/m}$ on X_{NaCleq}, even for systems with significant fH_2S (Fig 4). As we used the same Cu-
787 Au alloy composition as Zajacz et al. (2011), we can then compare the Cu concentration
788 range of the silicate melt in our runs to the Cu content of pure H_2O-H_2S fluids in Zajacz
789 et al. (2011) runs (~40 ppm Cu) to obtain the apparent partition coefficient between the
790 melt and Cl-free, H_2S-rich MVPs ($D_{Cu}^{f/m}$ ~ 1.5). However, given 1) the similar densities
791 and extremely low dielectric constant for the Cl-free vapor at both sets of conditions, and
792 2) the experiments of Zajacz et al. (2011) were conducted at 1000°C with more than
793 double the total sulfur in the volatile phase, Cu concentrations in MVPs will likely be

794 comparable or lower at 800°C and 100 or 200 MPa. Thus making this apparent $D_{Cu}^{f/m}$ ~
795 1.5 value a maximum for very low ∑Cl MVPs at our conditions.

796 Using this maximum value for [$NaCuHS_2$], the Cu concentration range in the melt
797 ($D_{Cu}^{f/m}$ ~ 1.5), and the previous fit and intercept for low H_2S Cu-Cl partitioning data (Eq
798 8) we can define Cu partitioning in the presence of H_2S as follows:

799 $$D_{Cu}^{f/m} = 8.0x10^4\left[\left(X_{NaCleq}\right)^2 * \left\{\left(X_{H_2O}\right)^{15} + K_9\left(X_{H_2S}\right)\left(X_{H_2O}\right)^{Y}\right\}\right] + 380\left(X_{NaCleq}\right) + 0.8 \qquad (13)$$

800 Following Equation (13) the additional partitioning capacity of H_2S-rich MVPs relies on
801 the equilibrium constant for Cl-HS exchange (K_9), the mole fraction of H_2S in the MVP
802 and the relevant solvation parameter for NaCuClHS (Y) which may be different than that
803 for $NaCuCl_2$ (Z). We have run an additional least squares regression using this
804 formulation to fit the available H_2S-rich experiments containing ~1.5 mol% H_2S (Figure
805 4 - yellow symbols) to yield the following combined equation for Cu partitioning;

806 $$D_{Cu}^{f/m} = 8.0(\pm1.4)x10^4\left[\left(X_{NaCleq}\right)^2 * \left\{\left(X_{H_2O}\right)^{14\pm2} + 180(\pm60)\left(X_{H_2S}\right)\left(X_{H_2O}\right)^{15\pm2}\right\}\right] + 380(\pm50)\left(X_{NaCleq}\right) + 0.8(\pm0.5) \qquad (14)$$

807 Equation (14) provides an excellent fit to the data with R_2= 0.95 and <25% relative
808 uncertainty on K_9 and Y fit parameters. The H_2S model fit returns a rather uncertain
809 intercept but the quality of the fit is very insensitive to the intercept value. The original
810 intercept from the low fH_2S dataset has been retained for simplicity. Thus, for the
811 unlikely case of salt-free degassing, additional data would be required to improve
812 Equation (14) to predict the limited Cu partitioning expected for such conditions.

813 Given the very similar Y and Z parameters for the influence of H_2O as a solvent
814 on the two ion-pair complexes we can apply a final simplification ($Y = Z$) to yield:

$$D_{Cu}^{f/m} = 8.0(\pm 1.4)x10^{4}\left[\left(X_{NaCleq}\right)^{2}\left(X_{H_2O}\right)^{14\pm 2}\left\{1+180(\pm 60)\left(X_{H_2S}\right)\right\}\right] + 380(\pm 50)\left(X_{NaCleq}\right) + 0.8(\pm 0.5) \quad (15)$$

This final Cu partitioning equation highlights the dominance of X_{NaCleq} on controlling Cu extraction from melts into MVPs, and excess Cu extracted into MVPs containing H_2S. The formation of the {(Na, K)CuClHS} complex is limited by both X_{NaCleq} and X_{H2S} and can, at most, roughly double Cu partitioning into MVPs at the maximum reasonable X_{H2S} (sulfide saturation) for reduced systems.

The maximum increase in Cu partitioning show in Fig (4) at maximum X_{H2S} is only valid for MVPs that are *already saturated* in magmatic Cu-Fe sulfides. Conversely, the presence of oxidized sulfur species (SO_2) has a negligible impact on the partitioning of copper, with partition coefficients indistinguishable from those from sulfur-free magmatic systems (Fig 4). In oxidized sulfurous MVPs magmatic SO_2, in much the same way as CO_2 (Tattitch et al. 2015), behaves as a "hard gas" and does not appear to act as a ligand for metal transport. Thus, in a magmatic system dominated by oxidized sulfur species, we should not expect any increase in Cu partitioning out of the melt and into vapors, brines, or supercritical fluids. Instead, efficient extraction and transport of Cu is controlled by $\sum$Cl or X_{NaCleq} in the MVPs and varies according to the competition between (Na,K)$CuCl_2$ and $CuCl^0$ complexation (Eq 8) with limited modification due to minor amounts of H_2S (Eq 15).

The influence of X_{NaCleq} and fO_2 on Molybdenum Partitioning

In a manner similar to Cu, MVPs may efficiently extract Mo, but, naturally, are limited by what is available from the melt, which in turn depends on the solubility of

837 molybdenite. Audétat et al. (2011) investigated the influence of temperature, fO_2, and
838 fS_2 on Mo concentrations at molybdenite saturation in natural systems. They showed that
839 at fixed fS_2 or at MSS/pyrrhotite saturation the Mo concentration of a melt increases with
840 increasing fO_2 due to the predominance of Mo^{6+} in the melt and Mo^{4+} in molybdenite. By
841 contrast, lower Mo concentrations in silicate melts at molybdenite saturation with
842 decreasing temperature are likely due to an increase in melt polymerization, which is
843 unfavorable to the highly coordinated Mo species in the melt. Our data provide a strong
844 experimental confirmation of the model of Audétat et al. (2011). The concentration of
845 Mo reported for our melts at 810 ^{o}C at reduced conditions (10-28 ppm Mo) and oxidized
846 conditions (43-59 ppm Mo) as well as the lower temperature (725^{o}C) oxidized run (10
847 ppm Mo) are all in excellent agreement with the model shown in Figure 5 of Audétat et
848 al. (2011). Yet while Mo concentrations in molybdenite-saturated melts may be well
849 constrained experimentally, the partitioning of Mo into MVPs is not.
850 The limited experimental data on Mo partitioning into MVP have provided
851 conflicting viewpoints of whether MVP chemistry has any control on the extent to which
852 Mo can be extracted from magmas. Candela and Holland (1984) suggest that Mo will
853 form "oxo-hydroxo" complexes and that these will be dominantly influenced by fO_2 and
854 temperature. Based on thermodynamic data, they argue that,Mo^{6+} will predominate in
855 fluids and thus complexes such as $MoO_2(OH)_2$ might be expected. However, their
856 experiments did not systematically examine a sufficient range in fO_2 to evaluate redox
857 control on the stability of such a complex. In contrast, Ulrich and Mavrogenes (2008)
858 suggest that for Mo-rich fluids there is a correlation between the solubility of Mo oxides
859 and the salinity or ∑Cl a MVP. On the basis of a logarithmic slope of ~0.78 for Mo

concentration versus ∑Cl they suggest that there is a roughly 1:1 ratio of Mo to Cl in the high temperature aqueous complex. This relationship would be in keeping with other molybdenum partitioning experiments at high salinity (Webster 1997) and high temperature (1300°C -1400°C and 1 GPa; MacKenzie and Canil 2011). However, the non-unity slope (~0.78), the high concentrations of Mo and the high uncertainty in the data suggest that more precise analysis is required to better establish the link between Cl and Mo. Finally, neither of these studies included sulfur as part of the magmatic assemblage and are thus at Mo concentrations far above molybdenite saturation.

Our data do not suggest any direct influence of reduced or oxidized volatile sulfur species on the partitioning of Mo at magmatic conditions. However, we can establish a strong link between $D_{Mo}^{f/m}$ and both X_{NaCleq} and redox state. There is a clear trend of increasing $D_{Mo}^{f/m}$ with increasing salinity and a separation between the experiments at reduced and oxidized conditions (Fig 6). If we regress the logarithmic correlation between $D_{Mo}^{f/m}$ and X_{NaCleq} for the oxidized and reduced experiments separately, both sets of experiments produced a 1:1 trend for Mo:Cl, indicating that a mono-chloride complex controls Mo partitioning. The low salinity end of the trend intersects the existing data for Mo partitioning into supercritical fluids at low to moderate salinity ($D_{Mo}^{f/m}$= 2.5 ± 1.6) of Candela and Holland (1984). At X_{NaCleq} >0.01 we suspect that that the salinity-dependant Mo complexes responsible for the increase were not retained in their quenched experimental fluids.

We speculate that any partitioning controlled by a salinity-dependent complex is similar to the formation of oxy-hydroxy Mo-complexes via partial substitution of (OH) for O in MoO_3 complexes in the melt according to the equilibrium:

883 $$MoO_3^{melt} + H_2O^{MVP} = MoO_2(OH)_2^{MVP} \quad (16)$$

884 The formation of a mono-chloride complex then involves simply replacing the
885 H_2O in the Mo complexes shown in equation (16) with a chloride ligand and allowing
886 Na^+, K^+ or H^+ to serve as a cation for an associated ion pair complex as follows:

887 $$MoO_3^{melt} + (Na,K,H)Cl^{MVP} = (Na,K,H)^+[MoO_3Cl]^- \quad (17)$$

888 We emphasize that the complex shown in equation (17) is only a schematic
889 representation of possible mono-chloride Mo complexes in MVPs. The high salinity end
890 of our trend for $D_{Mo}^{f/m}$ between reduced fluids and silicic melts is in excellent agreement
891 with high-temperature, 200 MPa partitioning data presented by Webster (1997) (Fig 6 –
892 filled circles). In the absence of definitive data on Cl as a complexing ligand we should
893 also consider the possibility that Na/K molybdate species are controlling salinity-
894 dependent complexation, e.g.:

895 $$\begin{aligned} A:&\quad MoO_2(OH)_2^{MVP} + NaCl = NaMoO_3(OH) + HCl \\ B:&\quad MoO_2(OH)_2^{MVP} + 2NaCl = Na_2MoO_4 + 2HCl \end{aligned} \quad (18)$$

896 (and equivalent expressions for KCl). However, the consistent slope of 1 on a logarithmic
897 plot of $D_{Mo}^{f/m}$ vs X_{NaCleq} suggests that if molybdates are controlling partitioning only the
898 first substitution of Na/K for H (Eq. 18A) is favoured across the entire salinity range. A
899 complexation involving 2 Na/K replacements (Eq. 18B) should have a 2nd order
900 dependence on X_{NaCleq}. The strong increase in overall partitioning of Mo with increasing
901 X_{NaCleq} would require that the Na/K molybdates are much more favourable complexes
902 than the H molybdates. Moreover, the consistent slope for $D_{Mo}^{f/m}$ vs. X_{NaCleq} across vapors,
903 supercritical fluids and brines with different fSO_2 also suggests that the elevated Mo
904 partitioning at oxidized conditions is a result of an increase in stability of the same mono-

chloride or Na/K molybdate complexes relative to the silicate melts rather than any direct role of SO_2 in Mo complexation.

Recent work by Zhang et al. (2012) also highlights the possibility that thiomolybdates (e.g. $NaHMoO_2S_2$) control the solubility of molybdenite in saline, sulfurous magmatic-hydrothermal fluids. They show that this complexation relies upon an equilibrium dependant on X_{NaCleq}, as well fO_2, which is shown below.

$$\begin{aligned} A:&\quad MoS_2 + H_2O + NaCl + \tfrac{1}{2}O_2 = NaHMoO_2S_2 + HCl \\ B:&\quad MoS_2 + H_2O + 2NaCl + \tfrac{1}{2}O_2 = Na_2MoO_2S_2 + 2HCl \end{aligned} \tag{19}$$

The complexation in equation 19A is more consistent with the data presented in this study as it will be both linearly dependent on X_{NaCleq} and have a more limited dependence on fHCl. Furthermore, Equation (19) includes an implicit dependence on fO_2 that is also observed in our data. The solubility data reported by Zhang et al. (2012) are also consistent with our data at oxidized conditions, while their data at higher and lower fS_2 at more reduced conditions suggests slightly higher molybdenite solubility but bracket our data. These can then be converted to a partitioning equilibrium by considering the solubility of molybdenite in the melt according to the expression:

$$MoS_2 + 2H_2O + \tfrac{1}{2}O_2 = MoO_3 + 2H_2S \tag{20}$$

By combining this expression with the equilibria presented by Zhang et al. (2012) for the mono-alkali complex (Equation 19A) we obtain equilibria for the partitioning of Mo between melt and fluid as thiomolybdate complexes in the MVP via either H_2S or, at oxidized conditions, via SO_2:

$$\begin{aligned} &A: MoO_3 + 2H_2S + NaCl = NaHMoO_2S_2 + H_2O + HCl \\ &B: MoO_3 + 2SO_2 + H_2O + NaCl = NaHMoO_2S_2 + HCl + 3O_2 \end{aligned} \tag{21}$$

These equilibria highlight the same linear dependence of molybdenum partitioning on X_{NaCleq}. However, the additional influences of H_2S, or SO_2 and O_2 are not readily observed in our dataset and thus confirmation of the complexes in Equation (21) would be required before further treatment.

Although Mo^{6+} is likely the most significant valence of molybdenum in the hydrous silicate melt, the stability of Mo^{4+} in the prevailing oxide and sulfide (MoO_2 and MoS_2 respectively) would suggest that at least some of the Mo in the melt is present as an $Mo^{IV}O_2$ component. Farges and Seiwert (2006) reported XAFS spectra for Mo in silicate melts/glass to show that dissolved H_2O increases the stability of MoO_2 $\{Mo(IV)O_6^{-8}\}$, and that significant dissolved sulfur can produce $Mo(IV,V,IV)O_nS_m^{-x}$, or $Mo(IV)S_4^{-4}$ components in the melt. They demonstrated that 30% or more of the total Mo is present as Mo^{4+} for higher temperature conditions with variable fO_2 covering the range examined here.

Although the exact speciation of Mo in the melt for our experimental conditions remains unclear, we should also consider partitioning involving lower Mo valences, such as:

$$Mo^{IV}O_2^{melt} + \tfrac{1}{2}O_2 + H_2O^{MVP} = MoO_2(OH)_2^{MVP} \quad (22)$$

$$Mo^{IV}O_2^{melt} + \tfrac{1}{2}O_2 + NaCl = NaMoO_3Cl \quad (23)$$

$$Mo^{IV}O_2^{melt} + H_2O^{MVP} + \tfrac{1}{2}O_2 + NaCl = NaMoO_3(OH) + HCl \quad (24)$$

To the extent that Mo is present as Mo(IV) or Mo(V) in the melt the fO_2 of the system will thus have an influence on partitioning. It is also possible that a different mono-chloride or sulfide complex, perhaps sensitive to fO_2, is responsible for the observed trends in the Mo partitioning data.

949 Despite these various caveats, given the available experimental data, we have
950 chosen to assume a $NaMoO_3Cl$ complexation mechanism and fit the Mo partitioning data
951 for reduced and oxidized fluids separately as functions of their salinity. Alternative
952 complexation via Na-K molybdates or Na-K-H thiomolybdates would retain a linear
953 dependence on X_{NaCleq}, but with additional terms for the influence of fHCl, $f H_2S$ or $f SO_2$
954 on the complex's stability.

955 If we examine and rearrange the equilibrium constants for equations (22) and (23)
956 we obtain:

957
$$K_{EQ22} = \frac{aMoO_2(OH)_2}{(aH_2O)(aMoO_3)} \qquad \frac{aMoO_2(OH)_2}{[Mo]^{melt}} = K_{EQ22}(aH_2O)$$
$$K_{EQ23} = \frac{aNaMoO_3Cl}{(aNaCl_{eq})(aMoO_3)} \qquad \frac{aNaMoO_3Cl}{[Mo]^{melt}} = K_{EQ23}(aNaCl_{eq}) \qquad (25)$$

958 The overall $D_{Mo}^{f/m}$ is then the sum of the oxy-hydroxy and mono-chloride or
959 thiomolybdate complexes:

960
$$[Mo]^{MVP} = \frac{aMoO_2(OH)_2 + aNaMoO_3Cl}{[Mo]^{melt}} \qquad (26)$$

961 Simplifying activities to mole fractions and combining these expressions yields $D_{Mo}^{f/m}$ as a
962 function of X_{H2O}, X_{NaCleq}, and $f O_2$:

963
$$D_{Mo}^{f/m} = K_{EQ22}(X_{H_2O}) + K_{EQ23}(X_{NaCleq}) \qquad (27)$$

964 Regardless of the exact complexation mechanism, we can match this equation with the
965 experimental and natural $D_{Mo}^{f/m}$ data for either reduced (~NNO+0.6) or oxidized
966 (~NNO+2) fluids. Using our experimental dataset and a single average value from

967 Candela and Holland (1984) for $D_{Mo}^{f/m} = 2.5(1.6)$ at $X_{NaCleq} = 0.001$ we have generated two
968 empirically fit expressions for $D_{Mo}^{f/m}$ vs X_{NaCleq} at reduced;

969 $$D_{Mo}^{f/m}\{NNO+0.6\} = 1.5(\pm 0.7)*\left(X_{H_2O}\right)+150(\pm 30)*\left(X_{NaCl_{eq}}\right) \quad (28)$$

970 and at oxidized conditions:

971 $$D_{Mo}^{f/m}\{NNO+2\} = 1.5(\pm 0.7)*\left(X_{H_2O}\right)+430(\pm 60)*\left(X_{NaCl_{eq}}\right) \quad (29)$$

972 Thse expression are in excellent agreement with the experiments at both conditions (R^2=
973 0.94 and 0.95 respectively with 20% and 15% relative uncertainty in the equilibrium
974 constant) as shown by the curved light blue and dark blue lines in Fig (6).

975 Our expression can be used to predict Mo partitioning over a large range of
976 conditions for felsic melts, although caution should be exercised outside the experimental
977 conditions. Equations (28) and (29) demonstrate that the salinity-dependent complexes
978 are roughly two orders of magnitude more favourable than oxy-hydroxy Mo complexes.
979 It is worth noting that although the derivation is shown for Na, our experimental data do
980 not provide any direct evidence as to which cation(s) dominate the Mo complexes (i.e.
981 Na^+, K^+, or H^+).

982 The data of Audétat and Pettke (2003) provide a test of the X_{NaCleq} dependence of
983 Mo partitioning. They measured Mo in co-genetic melt inclusions and vapor/brine fluid
984 inclusions from the Rito del Medio pluton, covering a range of salinities. Their measured
985 values match our experimental data for relatively oxidized fluids (Figure 6 open
986 diamonds). Additional data presented by Zajacz et al. (2008) from the Ehrenfriedersdorf
987 (Erzgebirge Mtns.), Rito del Medio (Mexico), and Mt. Malosa (Malowi) systems,
988 Audétat (2010) from the Cave Peak Mo-Nb deposit (Texas) and by Audétat et al. (2008)

989 from the Stronghold Granite (Arizona) cover a smaller salinity range and are more
990 scattered, but again are all broadly consistent with the salinity-dependent trends for
991 oxidized magmatic fluids. A limited amount of data from the Cuasso al Monte (Italy) and
992 minor parts of Mt. Malosa show somewhat muted Mo partitioning into the MVPs, more
993 consistent with only oxy-hydroxy complexation of Mo; it remains unclear why these
994 systems do not seem to show the expected X_{NaCleq}-dependence (Zajacz et al. 2008).
995 Given the 1:1 correlation between Mo and X_{NaCleq} across the full range of salinity
996 examined we predict, as for Cu, that brine/vapor partitioning will follow the same trends.
997 When we examine the data for brine/vapor partitioning from natural systems, the
998 majority show $D_{Mo}^{b/v}$ directly proportional to the ratio of chloride in brine to that in vapor
999 ($\sum Cl^{b/v}$), in the same manner observed in our experiments. Analysis of coexisting brine
1000 and vapor fluid inclusions from the Questa Mo deposit (Klemm et al. 2008), Cave Peak
1001 Mo-Nb deposit (Audétat 2010), and Grasberg Cu-Au deposit (Heinrich et al. 1999) all
1002 show $D_{Mo}^{b/v} = D_{Cl}^{b/v}$ within the analytical uncertainty. Additional data from the Treasure
1003 Mountain dome and Drammen granite (Lerchbaumer and Audétat 2012) also show an
1004 increase in Mo concentrations with increasing salinity, albeit with a very large range in
1005 absolute concentrations for different samples within the same system. We conclude that
1006 salinity-dependent complexes play an important role in Mo extraction from melts, and
1007 that our expression for $D_{Mo}^{f/m}$ as a function of X_{NaCleq} provides a good first estimate for
1008 modelling natural systems.
1009
1010 **IMPLICATIONS**

Understanding controls on the partitioning of Cu and Mo in the arc environment has long been viewed as critical to building genetic models for the formation of PCDs. Several recent studies have cast doubt upon what natural samples can tell us about Cu/Mo MVP partitioning (Lerchbaumer and Audétat 2012; Seo and Heinrich 2013), while others have proposed new reactive mechanisms for mineralization (Blundy et al. 2015; Henley at al. 2015; Richards (2016) and references therein; van Hinsberg et al. 2016) that draw upon a broader range of the MVPs known to flux through arc magmatic systems. Our study provides a more comprehensive picture of magmatic Cu and Mo partitioning, covering the spectrum of pressure, temperature, salinity ($\sum$Cl), oxidation environment (fO_2), and sulfur content necessary to make reasonable predictions throughout the shallow arc crust. In addition, the compiled experimental dataset incorporates data produced by numerous independent studies of synthetic and natural systems showing the same behaviour for Cu and Mo across the range of conditions examined.

Our compilation of experimental data shows very clearly how $(Na,K,H)^{+}\{CuCl_2\}^{-}$ ion pair complexes and Cl partitioning control Cu partitioning in supercritical MVPs and, following phase separation, in magmatic vapors and brines. Reduced sulfur species have a subordinate influence on partitioning, while oxidise sulfur species show no discernible effect. The inability of SO_2 to impact Cu partitioning further complicates models for maintaining a simultaneously high Cu, Fe and S content in a magmatic vapor as it decompresses away from the parental magmas. Furthermore, new studies highlight the difficulty in obviating sulfide saturation through oxidation alone (Matjuschkin et al. 2016) indicating that Cu and S may be decoupled during MVP exsolution. New mechanisms for mineralization explore this idea of an external source for sulfur, avoiding

problems of co-enrichment of Cu, Fe and S into shallow melts, as well as highlighting that many barren intrusions may be those associated with "normal" Cu-Fe-Cl MVPs that did not receive a subsequent sulfur flux. In this scenario we must imagine superimposing mixing of MVPs from disparate sources within the wider magmatic system (Blundy et al. 2015) and reactive mineralization mechanisms (Henley et al. 2015) on the already complicated picture of degassing supercritical fluids and phase separation of metal-rich brines. In order to critically evaluate these new hypotheses against conventional mechanisms of PCD mineralization the next step is to construct models for fluid transport, storage, and mineralization across all MVP salinities using the quantitative Cl-dominated partitioning behaviour for Cu and Mo presented here.

The stability of Mo-oxy-hydroxy complexes in MVPs means that, unlike Cu, Mo will remain slightly compatible in the MVPs even at very low salinity, for the P-T conditions common to Mo porphyry deposits. During the early stages of MVP exsolution higher temperatures and lower salinities will favour a higher Mo/Cu ratio in the exsolved fluids compared to exsolution in later stages whereupon significant Cl enrichment in the melt through crystallisation (e.g. Candela and Piccoli 1997, 2005) and higher $D_{Cl}^{f/m}$ (e.g. Webster et al. 2014) will favour Cu partitioning over Mo. Thus the earliest exsolved fluids will have the highest Mo/Cu ratio during the lifetime of an intrusion.

Oxidized fluids of sufficient ∑Cl will also have a large potential for extracting Mo from silicate melts. Given the sharply decreasing equilibrium fS_2 at MoS_2 saturation (Audétat et al. 2011) with reduced fO_2, we speculate that, where reduced sulfur is available (via H_2S or reaction of SO_2 to produce S^{6+} and S^{2-}), an MVP will precipitate molybdenite until the available Mo is exhausted before any precipitaiton of Cu-Fe

sulfides at higher fS_2. However, given that complexation of Mo as mono-chlorides, molybdates, or thiomolybdates would all be broadly consistent with our data, we feel that more direct characterization of MVP Mo complexation is required before elaborating on interpretations of Mo transport and mineralization. Nonetheless, establishing the empirical relationship between Cl and S for transport and mineralization of Mo vs. Cu is critical to reconcile the observation that Mo mineralization is distinct from Cu-Au or simple Cu mineralization in many porphyry deposits (e,g, Proffett 2003; Rusk et al. 2008; Wilson et al. 2003).

Extrapolating the Cl-dependence of Cu and Mo partitioning to greater depths of MVP release requires a detailed study of Cl partitioning as a function of pressure and melt composition. While early studies suggest that Cl may partition strongly into MVPs during early/deep degassing (Shinohara 1994), these data are in conflict with the increased compatibility of Cl in less evolved melts (Zajacz et al. 2012) and the observation of Cl-rich and S-poor, evolved, low pressure melt inclusions in many natural volcanic systems (e.g. Blundy et al 2008 USGS Prof Pap). Our data for $D_{Cl}^{f/m}$ show that Cl partitioning has a strong dependence on the exsolving fluid salinity (or $\sum$Cl) and that Cl becomes more compatible in peralkaline melts. In order to deconvolve these effects from the effects of pressure and melt composition more broadly, additional experimental work is required. In either case reduced Cl partitioning into the MVPs will limit Cu and Mo extraction. Thus shallow intrusions of metaluminous to slightly peraluminous magmas rich in Cl, consistent with observed trends in volcanic systems, are likely the most conducive to efficient Cu and Mo extraction.

Once MVPs exsolve from their parent magma decompression will lead to phase separation and the condensate brines will sequester Cu and Mo. Mixing with CO_2 could lead to mineralization of some metals due to its ability to reduce ore mineral solubility (Van Hinsberg et al. 2016) or to enhance formation of hyper-saline metal-rich brines (Tattitch et al. 2015). Some systems may avoid significant brine saturation over some of the hypogene ore zone (e.g. Butte PCD; Rusk et al. 2004) by mineralizing at great depth from a single supercritical fluid of sufficient salinity and Fe-Cu-Mo-Au content to source metals for the hypogene ore. However, the abundance of brine inclusions (e.g. Bodnar et al., 2014) and the prevalence of brecciation features in many PCDs (e.g. Sillitoe, 2010; Sinclair, 2007) suggests that formation of dense brines and the ascent of low density Cu-poor vapors up and away from the ore zone is common. The relatively high density (and viscosity) of metal-rich brines confers upon them transport properties similar to those of immiscible melts, thus more quantitative understanding of their formation, transport and storage in the shallow crust is paramount. Numerical models of this process (Fournier, 1999; Weis, 2015) demonstrate the viability of trapping of brines in lenses above shallow intrusions. Our experimental data and partitioning models enable the behaviour of Cu and Mo in such complex, dynamic systems to be investigated quantitatively.

Acknowledgements

We would like to thank Dr. Robert Bodnar and Dr. Luca Fedele for use and assistance with the LA-ICPMS laboratory at Virginia Tech for fluid inclusion analyses. We would like to thank Dr. Richard Brooker and Charles Clapham for assistance in upgrading the hydrothermal laboratory at University of Bristol to make this research possible. We would like to thank Andreas Audétat and an anonymous reviewer for many

1102 helpful comments and suggestions. Finally, we would like to thank Robert Loucks and
1103 Cyril Chelle-Michou for helpful comments on earlier drafts. This research was funded as
1104 part of the collaborative Bristol – BHP Billiton porphyry copper project.

1105

1106

References

Annen C., Blundy J. D., and Sparks R. S. J. (2006) The genesis of intermediate and silicic magmas in deep crustal hot zones. Journal of Petrology 47, 505-539.

Anthony, A., Reynolds, J., Beane, R., (1984) Identification of daughter minerals in fluid inclusions using scanning electron microscopy and energy dispersive analysis. American Mineralogist, 69, 1053-1057

Audétat A. (2010) Source and Evolution of Molybdenum in the Porphyry Mo(-Nb) Deposit at Cave Peak, Texas. Journal of Petrology, 51, 1739-1760

Audétat A., and Simon A.C. (2012) Magmatic controls on porphyry copper genesis. Economic Geology Special Publication 16, Ch 10

Audétat, A., and Pettke, T. (2003) The magmatic-hydrothermal evolution of two barren granites: A melt and fluid inclusion study of the Rito del Medio and Canada Pinabete plutons in northern New Mexico (USA) Geochimica et Comsmochimica Acta, 67, 97-121

Audétat A., Dolejs D., Lowenstern J. B. (2011) Molybdenite Saturation in Silicic Magmas: Occurrence and Petrological Implications. Journal of Petrology, 52, 891-904

Audétat A., Pettke T., Heinrich C. A., and Bodnar R. J. (2008) The Composition of Magmatic-Hydrothermal Fluids in Barren and Mineralized Intrusions. Economic Geology, 103, 877-908.

Audétat A., Gunther D., and Heinrich C. A. (1998) Formation of a magmatic-hydrothermal ore deposit: Insights with LA-ICP-MS analysis of fluid inclusions. Science, 279, 2091-2094.

1130 Barton P.B. (1973) Solid Solutions in the system Cu-Fe-S. Part I: The Cu-S and CuFe-S
1131 joins. Economic Geology, 68, 455-465
1132 Bodnar, R. J., Lecumberri-Sanchez, P., Moncada, D., Steele-MacInnis, M. (2014) Fluid
1133 inclusions in hydrothermal ore deposits. *Treatise on Geochemistry* (2nd Ed), *Ch.*
1134 *13.5*, 119-142
1135 Bodnar R.J., Sterner S.M. and Hall, D.L. (1989) SALTY: a FORTRAN program to
1136 calculate compositions of fluid inclusions in the system NaCl-KCl-H_2O.
1137 Computers & Geosciences, 15, 19-41.
1138 Bodnar R. J., Burnham C. W., and Sterner S. M. (1985) Synthetic fluid inclusions in
1139 natural quartz. 3.Determination of phase-equilibrium properties in the system
1140 H_2O-NaCl to 1000-degrees-C and 1500 bars. Geochimica et Cosmochimica Acta,
1141 49, 1861-1873.
1142 Candela P. A. and Piccoli P. M. (2005) Magmatic processes in the development of
1143 porphyry-type ore systems. Economic Geology 100th Anniversary Volume, 25-
1144 38.
1145 Candela P. A. and Piccoli P. M. (1997) A review of shallow ore-related granites:
1146 Textures, volatiles and ore metals Journal of Petrology, 38, 1619-1633.
1147 Candela P. A. and Holland H. D. (1984) The partitioning of copper and molybdenum
1148 between silicate melts and aqueous fluids. Geochimica et Cosmochimica Acta,
1149 48, 373-380.
1150 Cashman K, and Blundy J. (2000) Degassing and crystallization of ascending andesite
1151 and dacite. Philisophical Transactions of the Royal Society of London, 358, 1487-
1152 1513

1153 Chou I. M. (1987) Oxygen buffer and hydrogen sensor techniques at elevated pressures
1154 and temperatures. Hydrothermal Experimental Techniques, Ch. 3, 61-98.
1155 Churakov S. V. and Gottschalk M. (2003) Perturbation theory based equation of state for
1156 polar molecular fluids: II. Fluid mixtures. Geochimica et Cosmochimica Acta, 67,
1157 2415-2425.
1158 Clemente B., Scaillet B., and Pichavant M. (2004) The solubility of sulphur in hydrous
1159 rhyolitic melts. Journal of Petrology, 45, 2171-2196.
1160 Deubener J., Muller R., Behrens H. and Heide G. (2003) Water and the glass transition
1161 temperature of silicate melts. Journal of Non-Crysaline Solids, 330, 268–273.
1162 Driesner T., Heinrich C.A. (2007) The system H_2O–NaCl. Part I: Correlation formulae
1163 for phase relations in temperature–pressure–composition space from 0 to 1000°C,
1164 0 to 5000bar, and 0 to 1 XNaCl. Geochimica et Cosmochimica Acta, 71, 4880-
1165 4901
1166 Farges F. and Siewert R. (2006) Structural evironments around molybdenum in silicate
1167 glasses and melts. II. Effect of temperature, pressure, H_2O, halogens and sulfur.
1168 The Canadian Mineralogist, 44, 755-773
1169 Field C.W., Zhang L., Dilles J.H., Rye R.O., Reed M.H. (2005) Sulfur and oxygen
1170 isotopic record in sulfate and sulfide minerals of early, deep, pre-Main Stage
1171 porphyry Cu–Mo and late Main Stage base-metal mineral deposits, Butte district,
1172 Montana, Chemical Geology, 215, 61-93
1173 Fournier, R.O. (1999) Hydrothermal processes related to movement of fluid from plastic
1174 into brittle rock in the magmatic-epithermal environment. Economic Geology, 94,
1175 1193-1211

1176 Frank M. R., Simon A. C., Pettke T., Candela P. A., and Piccoli P. M. (2011) Gold and
1177 copper partitioning in magmatic-hydrothermal systems at 800 degrees C and 100
1178 MPa. Geochimica et Cosmochimica Acta, 75, 2470-2482.
1179 Gunther D., Audétat A., Frischknecht R., and Heinrich C. A. (1998) Quantitative analysis
1180 of major, minor and trace elements in fluid inclusions using laser ablation
1181 inductively coupled plasma mass spectrometry. Journal of Analytical Atomic
1182 Spectrometry, 13, 263-270.
1183 Hattori K. H. and Keith J. D. (2001) Contribution of mafic melt to porphyry copper
1184 mineralization: evidence from Mount Pinatubo, Philippines, and Bingham
1185 Canyon, Utah, USA. Mineralium Deposita, 36, 799-806.
1186 Heinrich C. (2005) The physical and chemical evolution of low-salinity magmatic fluids
1187 at the porphyry to epithermal transition: a thermodynamic study. Mineralium
1188 Deposita, 39, 864-889.
1189 Heinrich C. A., Driesner T., and Landtwing M. R. (2004) Boiling, condensation and
1190 vapour contraction in magmatic-hydrothermal Cu-Au ore systems. Geochimica et
1191 Cosmochimica Acta, 68, A295-A295.
1192 Heinrich C. A., Pettke T., Halter W. E., Aigner-Torres M., Audétat A., Gunther D.,
1193 Hattendorf B., Bleiner D., Guillong M. and Horn I. (2003) Quantitative multi-
1194 element analysis of minerals, fluid and melt inclusions by laser-ablation
1195 inductively-coupled- plasma mass-spectrometry. Geochimica et Cosmochimica
1196 Acta, 67, 3473–3497.

1197 Heinrich C. A., Gunther D., Audétat A., Ulrich T., and Frischknecht R. (1999) Metal
1198 fractionation between magmatic brine and vapor, determined by microanalysis of
1199 fluid inclusions. Geology, 27, 755-758.
1200 Heinrich C.A., Ryan C.G., Mernagh T.P., Eadington P.J. (1992) Segregation of ore
1201 metals between magmatic brine and vapor; a fluid inclusion study using PIXE
1202 microanalysis. Economic Geology, 87, 1566-1583
1203 Henley R. W., King P.L., Wykes J.L., Renggli C.J., Brink F.J., Clark D.A., Troitzsch U.
1204 (2015) Porphyry copper deposit formation by sub-volcanic sulphur dioxide flux
1205 and chemisorption. Nature Geoscience, 8, 210-215
1206 Humphreys, M.C.S., Kearns, S.L., Blundy, J.D. (2006) SIMS investigation of electron-
1207 beam damage to hydrous, rhyolitic glasses: Implications for melt inclusion
1208 analysis. American Mineralogist, 91, 667-679
1209 John D. A., Ayuso R. A., Barton M. D., Blakely R. J., Bodnar R. J., Dilles J. H., Gray F.,
1210 Graybeal F. T., Mars J. C., McPhee D. K., Seal R. R., Taylor R. D., and Vikre P.
1211 G. (2010) Porphyry copper deposit model, chap. B of Mineral deposit models for
1212 resource assessment. U.S. Geological Survey Scientific Investigations Report
1213 2010–5070–B, 1-169.
1214 Jugo, P.J., Wilke M., Botcharnikov R.E. (2010) Sulfur K-edge XANES analysis of
1215 natural and synthetic basaltic glasses: Implications for S speciation and S content
1216 as function of oxygen fugacity. Geochimica et Cosmochimica Acta, 74, 5926-
1217 5938.
1218 Jugo P. J., Candela P. A., and Piccoli P. M. (1999) Magmatic sulfides and Au : Cu ratios
1219 in porphyry deposits: an experimental study of copper and gold partitioning at 850

degrees C, 100 MPa in a haplogranitic melt pyrrhotite intermediate solid solution gold metal assemblage, at gas saturation. Lithos, 46, 573-589.

Keppler, H., and Wyllie, P. (1991) Partitioning of Cu, Sn, Mo, W, U, and Th between melt and aqueous fluid in the systems haplogranite-H_2O-HCl and haplogranite-H_2O-HF. Contributions to Mineralogy and Petrology, 109, 139-150

Klemm L. M., Pettke T. and Heinrich C. A. (2008) Fluid and source magma evolution of the Questa porphyry Mo deposit, New Mexico, USA. Mineralum Deposita, 43, 533–552.

Kodera, P., Murphy, P.J., Rankin, A.H., (2003) Retrograde mineral reactions in saline fluid inclusions: The transformation ferropyrosmalite <-> clinopyroxene. American Mineralogist, 88, 151-158.

Lerchbaumer L. and Audétat A. (2013) The Metal Content of Silicate Melts and Aqueous Fluids in Subeconomically Mo Mineralized Granites: Implications for Porphyry Mo Genesis, Economic Geology, 108, 967-1013.

Lerchbaumer L. and Audétat A. (2012) High Cu concentrations in vapor-type fluid inclusions: An artifact? Geochimica et Cosmochimica Acta, 88, 255-274.

Lee, C., Luffi, P., Chin, E., Bouchet, R., Dasgupta, R., Morton, D., Roux, V., Yin, Q., Jin, D., (2012) Copper systematics in arc magmas and implications for crust-mantle differentiation. Science, 336, 64-68

Lowenstern J. B. (2001) Carbon dioxide in magmas and implications for hydrothermal systems. Mineralium Deposita, 36, 490-502.

Lowenstern J., (2000) A review of the contrasting behavior of two magmatic volatiles: chlorine and carbon dioxide, Journal of Geochemical Exploration, 69, 287-290

1243 Masotta, M., Keppler, H., Chaudhari, A. (2016) Fluid-melt partitioning of sulfur in
1244 differentiated arc magmas and the sulfur yield of explosive volcanic eruptions
1245 Geochimica et Cosmochimica Acta, 176, 27-43.
1246 Mei, Y., Sherman, D., Liu, W. and Brugger, J. (2013) Ab initio molecular dynamics
1247 simulation and free energy exploration of copper(I) complexation by chloride and
1248 bisulfide in hydrothermal fluids. Geochimica et Cosmochimica Acta, 102, 45-64.
1249 Mengason M.J., Piccoli P.M., Candela P. (2010) An evaluation of the effect of copper on
1250 the estimation of sulfur fugacity (fS_2) from pyrrhotite composition. Economic
1251 Geology, 105,1163-1169
1252 Mutchler S., Fedele L., and Bodnar R. (2008) Analysis Management System (AMS) for
1253 reduction of laser ablation ICPMS data. . Laser-Ablation-ICPMS in the Earth
1254 Sciences: Current Practices and Outstanding Issues (P. Sylvester, ed.)
1255 Mineralogical Association of Canada Short Course Series 40, 318-327.
1256 Nagaseki H. and Hayashi K.-i. (2008) Experimental study of the behavior of copper and
1257 zinc in a boiling hydrothermal system. Geology, 36, 27-30.
1258 Newman S. and Lowenstern J. B. (2002) VOLATILECALC: a silicate melt-H_2O-CO_2
1259 solution model written in Visual Basic for excel. Computers & Geosciences, 28,
1260 597-604.
1261 Pettke T., Oberli F. and Heinrich C. A. (2010) The magma and metal source of giant
1262 porphyry-type ore deposits, based on lead isotope microanalysis of individual
1263 fluid inclusions. Earth and Planetary Science Letters, 296, 267–277.

1264 Pokrovski G. S., Borisova A.Y., and Harrichoury J. C. (2008) The effect of sulfur on
1265 vapor-liquid fractionation of metals in hydrothermal systems. Earth and Planetary
1266 Science Letters, 266, 345-362.
1267 Redmond P. B., Einaudi M. T., Inan E. E., Landtwing M. R., and Heinrich C. A. (2004)
1268 Copper deposition by fluid cooling in intrusion-centered systems: New insights
1269 from the Bingham porphyry ore deposit, Utah. Geology, 32, 217-220.
1270 Richards J. (2016) Clues to hidden copper deposits, Nature geoscience, 9, 195-196
1271 Ripley, E., Brophy, J., Li, C. (2002) Copper Solubility in a basaltic melt and sulfide
1272 liquid/silicate melt partition coefficients of Cu and Fe. Geochimica et
1273 Cosmochimica Acta, 66, 2791-2800
1274 Roedder, E. (1971) Fluid inclusion studies on the porphyry-type ore deposits at Bingham,
1275 Utah, Butte, Montana, and Climax, Colorado. Economic Geology, 66, 98-120
1276 Rusk B. G., Reed M. H., and Dilles J. H. (2008) Fluid inclusion evidence for magmatic-
1277 hydrothermal fluid evolution in the porphyry copper-molybdenum deposit at
1278 Butte, Montana. Economic Geology, 103, 307-334.
1279 Rusk B. G., Reed M. H., Dilles J. H., Klemm L. M., and Heinrich C. A. (2004)
1280 Compositions of magmatic hydrothermal fluids determined by LA-ICP-MS of
1281 fluid inclusions from the porphyry copper-molybdenum deposit at Butte, MT.
1282 Chemical Geology, 210, 173-199.
1283 Seo, J. H. & Heinrich, C. A. (2013) Selective copper diffusion into quartz-hosted vapor
1284 inclusions: Evidence from other host minerals, driving forces, and consequences
1285 for Cu–Au ore formation. Geochimica et Cosmochimica Acta, 113, 60–69.
1286 Sillitoe R. H. (2010) Porphyry Copper Systems. Economic Geology, 105, 3-41.

1287 Simon A. C. and Ripley E. M. (2011) The Role of Magmatic Sulfur in the Formation of
1288 Ore Deposits. In: Sulfur in Magmas and Melts: Its Importance for Natural and
1289 Technical Processes (Eds. Behrens, H. and Webster, J. D. Eds.) 513-578.
1290 Simon A. C., Pettke T., Candela P. A., Piccolli P. M., and Heinrich C. A. (2006) Copper
1291 partitioning in a melt-vapor-brine-magnetite-pyrrhotite assemblage. Geochimica
1292 et Cosmochimica Acta, 70, 5583-5600.
1293 Sinclair W. D. (2007) Porphyry deposits, in Goodfellow, W.D., ed., Mineral Deposits of
1294 Canada: A Synthesis of Major Deposit-Types, District Metallogeny, the Evolution
1295 of Geological Provinces, and Exploration Methods. Geological Association of
1296 Canada, Mineral Deposits Division, Special Publication No. 5, 223-243.
1297 Sisson T.W. and Grove T.L. (1993) Experimental investigations of the role of H_20 in
1298 calc-alkaline differentiation and subduction zone magmatism. Contributions to
1299 Mineralogy and Petrology, 113, 143-166
1300 Sisson T.W., Ratajeski K., Hankins W.B., and Glazner A.F. (2005) Voluminous granite
1301 magmas from common basaltic sources. Contributions to Mineralogy and
1302 Petrology, 148, 635-661
1303 Sterner S. M. and Bodnar R. J. (1991) Synthetic fluid inclusions .10. Experimental-
1304 determination of P-V-T-X properties in the CO_2-H_2O system to 6-kb and 700-
1305 degrees-C. American Journal of Science, 291, 1-54.
1306 Sun R., and Dubessy J. (2012) Prediction of vapor–liquid equilibrium and PVTx
1307 properties of geological fluid system with SAFT-LJ EOS including multi-polar
1308 contribution. Part II: Application to H_2O–NaCl and CO_2–H_2O–NaCl System,
1309 Geochimica et Cosmochimica Acta, 88, 130-145

1310 Sun W., Audétat A., Dolejs D. (2014) Solubility of molybdenite in hydrous granitic melts
1311 at 800°C, 100-200 MPa, Geochimica et Cosmochimica Acta, 131, 393-401
1312 Tattitch B.C., Candela P.A., Piccoli P.M., Bodnar R.J. (2015) Copper partitioning
1313 between felsic melt and H_2O-CO_2 bearing saline fluids, Geochemica Et
1314 Cosmochimica Acta, Vol 148, pp 81-99
1315 Taylor J. R., Wall V. J., and Pownceby M. I. (1992) The calibration and application of
1316 accurate redox sensors. American Mineralogist 77, 284-295.
1317 Ulrich T., Gunther D., and Heinrich C. A. (1999) Gold concentrations of magmatic brines
1318 and the metal budget of porphyry copper deposits. Nature, 399, 676-679.
1319 Ulrich T. and Mavrogenes J. (2008) An experimental study of the solubility of
1320 molybdenum in H_2O and KCl-H_2O solutions from 500 degrees C to 800 degrees
1321 C, and 150 to 300 MPa. Geochimica et Cosmochimica Acta, 72, 2316-2330.
1322 van Zalinge M.E., Sparks R.S.J., Cooper F.J., Condon D.J. (2016) Early Miocene large-
1323 volume ignimbrites of the Oxaya Formation, Central Andes. Journal of the
1324 Geological Society, 173, 716-733
1325 Webster J.D. (1997) Exsolution of magmatic volatile phases from Cl-enriched
1326 mineralizing granitic magmas and implications for ore metal transport.
1327 Geochimica et Cosmochimica Acta, 61, 1017–1029
1328 Webster J.D., Goldoff B., Sintoni M.F., Shimizu N., and DeVivo B. (2014) C-O-H-Cl-S-
1329 F Volatile Solubilities, Partitioning, and Mixing in Phonolitic-Trachytic Melts and
1330 Aqueous9Carbonic Vapor±Saline Liquid at 200 MPa, Journal of Petrology, 55,
1331 2217-2248

1332 Webster J.D., Goldoff B., Shimizu N. (2011) C-O-H-S fluids and granitic magma: how S
1333 partitions and modifies CO2 concentrations of fluid-saturated felsic melt at 200
1334 MPa. Contributions to Mineralogy and Petrology, 162, 849-865
1335 Webster J. D. and Holloway J. R. (1988) Experimental constraints on the partitioning of
1336 Cl between topaz rhyoltite melt and H_2O and $H_2O + CO_2$ fluids - New
1337 implications for granitic differentiation and ore deposition. Geochimica et
1338 Cosmochimica Acta, 52, 2091-2105.
1339 Weis P. (2015) The dynamic interplay between saline fluid flow and rock permeability in
1340 magmatic-hydrothermal systems. Geofluids, 15, 350-371
1341 Whitney J.A. (1984) Fugacities of sulfurous gases in pyrrhotite-bearing silicic magmas.
1342 American Mineralogist, 69, 69-78
1343 Williams T. J., Candela P. A., and Piccoli P. M. (1997) Hydrogen-alkali exchange
1344 between silicate melts and two-phase aqueous mixtures: an experimental
1345 investigation. Contributions to Mineralogy and Petrology, 128, 114-126.
1346 Williams T. J., Candela P. A., and Piccoli P. M. (1995) The partitioning of copper
1347 between silicate melts and 2-phase aqueous fluids - An experimental investigation
1348 at 1-kbar, 800-degrees-C and 0.5-kbar, 850-degrees-C. Contributions to
1349 Mineralogy and Petrology 121, 388-399.
1350 Zajacz, Z. (2015) The effect of melt composition on the partitioning of oxidized sulfur
1351 between silicate melts and magmatic volatiles, Geochimica et Cosmochimica
1352 Acta, 158, 233-244
1353 Zajacz Z., Seo J. H., Candela P. A., Piccoli P. M., and Tossell J. A. (2011) The solubility
1354 of copper in high-temperature magmatic vapors: A quest for the significance of

various chloride and sulfide complexes. Geochimica et Cosmochimica Acta, 75, 2811-2827.

Zajacz Z., Hanley J., Heinrich C. A., Halter W. E., and Guillong M. (2009) Diffusive reequilibration of quartz hosted silicate melt and fluid inclusions: Are all metal concentrations unmodified? Geochimica et Cosmochimica Acta, 73, A1496-A1496.

Zajacz Z., Halter W.E., Pettke T., Guillong M. (2008) Determination of fluid/melt partition coefficients by LA-ICPMS analysis of co-existing fluid and silicate melt inclusions: Controls on element partitioning. Geochimica et Cosmochimica Acta, 72, 2169-2197

Figure 1: Schematic of the experimental capsule design. A custom alloyed Cu_3Au_{97} capsule is loaded with silicate glass, aqueous solution, molybdenite (Mb), magnetite (Mt) and variable amounts of pyrrhotite (Po) and chalcopyrite (Ccp) depending on reduced or oxidized conditions. The capsule is sealed and loaded in a Nimonic alloy cup and connected to an external magnetic filler rod control system. At run conditions the experiment yields a silicate magma and a magmatic volatile assemblage that contains either H_2S or SO_2+anhydrite. Quartz cores with longitudinal grooves (for fluid migration) keep the oxides/sulfides physically separate from the magma to improve analyses and serve to trap samples of the MVP(s) as fluid inclusions after in-situ fracturing.

Figure 2:
SEM images of run products from experiments at 200 MPa (A,B) and 100 MPa (C,D) at reduced (A,C) and oxidized (B,D) conditions. Experiments conducted at 200 MPa show much lower crystallinity due to lower H2O saturated liquidus. Biotite (Bt), clinopyroxene (Cpx), magnetite (Mt) and apatite (Ap) are present in these runs as well as either chalcopyrite (Ccp) or anhydrite (Anh) at reduced and oxidized conditions respectively. At lower pressure and higher crystallinity the same assemblage is observed except that Cpx is quite rare and instead amphibole (Hbl), plagioclase (Pl), and alkali feldspar (Ksp) are present. All of the experiments are also quartz (Qtz) saturated due to the experiment design.

Figure 3:
Photomicrographs of fluid inclusions from all experiment types. Inclusions are shown for both reduced (above) and oxidized (below) experiments with increasing salinity to the right. With increasing salinity, the density of the fluid increases and so the contraction bubble size decreases. Experiments at 100 MPa produced brine inclusions that also contain daughter mineral halite and sylvite (E, K, L). At reduced conditions all the inclusions contain chalcopyrite (Ccp) and intermediate to high salinity inclusions (C, D, E) also contain molybdenite (Mb). At oxidized conditions no Ccp is observed but instead a transparent phase, inferred to be a sulphate, is present. Here again, intermediate to high salinity inclusions (I, J, K) contain molybdenite.

Figure 4:
Compilation of copper partitioning data between a MVP and silicate melt ($D_{Cu}^{f/m}$) from our experiments as well at numerous other studies. Data for sulfur-free and low fH_2S experiments is shown in black-filled symbols.. These data show a clear trend of $D_{Cu}^{f/m}$ increasing with increasing X_{NaCleq}, due to the varied stability of both $CuCl^0$ (1:1 Cu:Cl - dashed line), and "excess" Cu due to $(Na,K)CuCl_2$ (1:2 Cu:Cl) complexation. The solid green line shows the empirical fit of these data assuming these complexation mechanisms and provides equilibrium constants to determine $D_{Cu}^{f/m}$ at any salinity. Quenched-fluid data from Candela and Holland (1984), shown in black crosses, follows the infered trend for $CuCl^0$ only and is not included in the fit (see text). In addition, H_2S-rich experiments are shown in yellow filled symbols and a similar fit (dotted line) for the additional contribution of (Na,K)CuCl(HS), and minimal $(Na,K)Cu(HS)_2$ complexation (See

text for fit equations and derivation). The empirical fit of the data based on the equilibrium between these complexes and the melt is shown in the top left.

Figure 5:
Compilation of copper partitioning data between coexisting brine and vapor from experiments as well as natural, topaz-hosted, fluid inclusions from the Mole Granite. Data for sulfur-free and low fH_2S experiments (black filled symbols) clearly shows the 1:1 correlation between D_{Cu} and D_{Cl} between the coexisting phases. H_2S-rich MVPs show a deviation towards the vapor phase, but under no conditions does the Cu favour the vapor over the brine. In addition, the data from natural topaz-hosted inclusions (average with 2σ error bars for all data) clearly fall directly on the line for the oxidized, or S-poor, brine-vapor partitioning data. This is in contrast to existing quartz-hosted data, which would plot low off the figure due to post-entrapment modification of vapor-rich inclusions.

Figure 6:
Compilation of molybdenum partitioning data between MVPs and silicate melts from experiments, molybdenum deposits and granitic plutonic systems. Both reduced experiments and oxidized experiments show a trend of increasing D_{Mo} with increasing salinity transitioning from a $MoO_2(OH)_2$ dominated system to one controlled by a salinity dependant complex such as $(Na,K)MoO_3Cl$ or $(Na,K)MoO_3(OH)$ or $(Na,K)HMoO_2S_2$ given the 1:1 Mo:Cl dependence over the majority of the data range. Our reduced experimental data (blue filled symbols) is in good agreement with limited datasets from older reduced experimental studies (black symbols). However, experiments at oxidized conditions (blue open symbols) are in good agreement with nearly all the data from natural systems (open symbols), with Mo partitioning roughly 2x greater than at reduced conditions. The empirical fits for the experimental data are shown in the top left.

Table 1: Cardones Ignimbrite pumice composition (wt%)

Na_2O	**2.7**
K_2O	**4.8**
CaO	**2.2**
FeO	**0.56**
MgO	**0.73**
MnO	**0.07**
TiO_2	**0.15**
Al_2O_3	**12.8**
SiO_2	**74.4**
ASI	**0.95**

Glass composition determined by ICP-EOS and contains 4.1wt% H_2O

Melt ASI moves from slightly peralkaline value shown to metaluminous when equilibrating with experimental aqueous fluid

Table 2: Reduced and Oxidized Experiment Conditions

Run	Duration (Hours)*	Temp (°C)	Pressure (MPa)	Log fO_2	Starting Glass (mg)	Na/K/H[◊] Solution (µl)	Starting Phases[S]
Reduced							
CMA201[r]	72*/120	810	100	NNO+0.5	10	10	G, Aq, Qtz, Ccp, Po, Mb
CMA406	72*/120	810	200	NNO+0.6	13	16	G, Aq, Qtz, Ccp, Po, Mb
CMA407	72*/120	810	200	NNO+0.7	14	15	G, Aq, Qtz, Ccp, Po, Mb
Oxidized							
CMA224[ox, r]	72*/120	810	100	NNO+2.0	11	10	G, Aq, Qtz, Mb, Po[d]
CMA303[ox, r]	72*/144	725	100	NNO+1.8	12	10	G, Aq, Qtz, Mb, Po[d]
CMA420[ox]	72*/120	810	200	NNO+1.8	15	16	G, Aq, Qtz, Mb, Po[d]
CMA421[ox]	96*/144	810	200	NNO+2.2	15	16	G, Aq, Qtz, Mb, Po[d]

*All experiments equilibrated at run conditions for 72 or 96 hours prior to in-situ fracturing

[◊] Aqueous starting solution: Na/K/H in a 10/10/1 ratio and 2.1 molal ∑Cl

[S] G=Rhyolite Glass, Aq=Aqueous Soln, Qtz=Quartz, Ccp=Chalcopyrite, Po=Pyrrhotite, Mb=Molybdenite,

[r] Cardones pumice also yielded minor relict Kspar, plagioclase, biotite, and clinopyroxene in lower P runs

[ox] Oxidized runs contain 3mg of crushed Ccp as a sulphur source which oxidized to SO_2 during run.

[d] Starting Po breaks down to generate SO_2 and anhydrite during oxidized runs

Table 3: Compositions of Reduced and Oxidized run product glasses: Shown in wt% (± 2σ)

RUN	n	Na_2O	K_2O	CaO	FeO	Al_2O_3	SiO_2	S (ppm)	Cl (ppm)	Cu (ppm)[L]	Mo (ppm)[L]	H_2O[s]	ASI
***Reduced { Log fO_2 = NNO + 0.6 }**													
CMA201	12	3.1 (0.3)	5.4 (0.1)	0.5 (0.1)	0.50 (0.07)	12.1 (0.4)	72.3 (0.8)	90 (60)	2400 (230)	19 (4)	10 (3)	4.6 (1.1)	1.02
CMA406[a]	21	2.9 (0.2)	5.1 (0.1)	1.0 (0.1)	0.62 (0.08)	12.7 (0.5)	70.0 (1)	88 (60)	2000 (140)	7 (1)	15 (3)	6.1 (0.7)	1.05
CMA407	21	2.7 (0.3)	4.9 (0.1)	1.0 (0.1)	1.10 (0.09)	12.2 (0.6)	70.6 (1.3)	86 (70)	1900 (150)	13 (5)	28 (7)	6.1 (0.7)	1.05
***Oxidized { Log fO_2 = NNO +2.0 }**													
CMA224	13	2.8 (0.2)	5.3 (0.2)	0.30 (0.04)	0.92 (0.05)	11.4 (0.3)	73.2 (0.7)	200 (80)	1500 (370)	28 (5)	43 (7)	4.8 (0.6)	1.04
CMA303	8	3.2 (0.3)	5.1 (0.2)	0.48 (0.1)	0.87 (0.08)	13.9 (0.9)	71.9 (1.5)	210 (120)	1300 (300)	27 (5)	10 (2)	4.4 (1)	1.19
CMA420	18	2.9 (0.2)	5.3 (0.1)	0.10 (0.02)	0.83 (0.06)	12 (0.6)	71.0 (1.1)	220 (100)	1500 (120)	17 (2)	59 (19)	6.3 (0.6)	1.11
CMA420	22	2.7 (0.3)	5.0 (0.2)	0.10 (0.03)	0.83 (0.07)	11.4 (0.7)	71.7 (1.6)	190 (100)	1500 (210)	12 (1)	52 (14)	6.9 (1.7)	1.13

‡ Minor components (MgO, TiO_2, MnO, P_2O_5) are below (0.2, 0.1, 0.1 and 0.05) wt% respectively in all runs

* Log fO_2 values calculated based on CoPd and NiPd sensors run with experiments (2σ = ± 0.2 log units)

[L] Cu and Mo concentrations are based on separate LA-ICPMS analyses (n > 5) run in tandem with fluid inclusion analyses

[a] Experiment CMA406 was run using a Cu_2Au_{98} capsule rather than the Cu_3Au_{97} alloy used for all other experiments

[s] H_2O values were also determined by SIMS analysis and are within 1σ of the water by difference values reported in this table

All experiments used Cardones Ignimbrite Pumice starting material

Table 4: LA-ICPMS Analysis of Fluid Inclusions from Reduced and Oxidized experiments (Na, K, Fe, Cu, Mo in ppm)

Run	FI Type	N	Microtherm[S,C]	($NaCl_{eq}$)*	X_{Cl}[m]	Na (±2σ)	K (±2σ)	Ca (±2σ)	Fe (±2σ)	Cu (±2σ)	Mo (±2σ)
Reduced { Log fO_2 = NNO + 0.6 }											
CMA201	Brine	14	220-225°C/ 365-370°C	61-62	0.33	109000 (6000)	180000 (13100)	23000 (11500)	129000 (46100)	6020 (1500)	690 (120)
CMA201	Vapor	11	-2 to -1.8 °C	3-3.5	0.01	2900 (1300)	4400 (2200)	720 (400)	3400 (1700)	650 (300)	25 (5)
CMA406[a]	Super Critical	21	-8 to -7.5 °C	12.5-13	0.044	17000 (2700)	27000 (5800)	2700 (1000)	17000 (7100)	2060 (460)	120 (30)
CMA407	Super Critical	12	-8 to -7.5 °C	12.5-13	0.044	17000 (2400)	29000 (4400)	1800 (380)	25000 (6700)	3300 (1250)	220 (50)
Oxidized { Log fO_2 = NNO + 2 }											
CMA224	Brine	15	210-215°C/ 365-375°C	61-62	0.33	115000 (12600)	145000 (24800)	37000 (18500)	96000 (34200)	5000 (1300)	5700 (2600)
CMA224	Vapor	12	-2 to -1.8 °C	3-3.5	0.01	4900 (1700)	7300 (2500)	1100 (600)	4300 (1800)	260 (140)	200 (60)
CMA303	Brine	8	260-270°C/ 330-335°C	53-54	0.26	90000 (67000)	113000 (44800)	29000 (13000)	75000 (30000)	4200 (1500)	1400 (110)
CMA303	Vapor	6	~ -3	5	0.016	9000 (3100)	11000 (9800)	4000 (2100)	3700 (550)	480 (220)	73 (36)
CMA420	Super Critical	12	-8 to -7.5 °C	12.5-13	0.044	12000 (1100)	20000 (3400)	690 (400)	12000 (3200)	2000 (440)	1300 (370)
CMA421	Super Critical	27	-8 to -7.5 °C	12.5-13	0.044	11700 (2400)	21000 (2200)	1100 (600)	16000 (3500)	1700 (400)	900 (220)

[S] Salt disappearance temperature ranges determined for brine inclusions (sylvite/halite)

[C] Ice melting temperature ranges determined for vapor and supercritical inclusions

* Salinity: NaCl equivalent units, shown in wt% ($CaCl_2$ and $FeCl_2$ counted as 1.5 salinity units)

[m] Total Chloride as mole fraction (X_{Cl} or X_{NaCleq}) inferred from Microthermometry and adjusted for Na/K/Ca/Fe

[a] Experiment CMA406 was run using a Cu_2Au_{98} capsule rather than the Cu_3Au_{97} alloy used for all other experiments

Table 5: Chlorine, Iron, Calcium, Copper and Molybdenum Partition Coefficients for Fluids (MVPs) and Melt

Run	FI Type	(Wt% $NaCl_{eq}$)	$X_{NaCleq}{}^{m}$	$D_{Cl}^{f/m}$	$D_{Fe}^{f/m}$	$D_{Ca}^{f/m}$	$D_{Cu}^{f/m}$	$D_{Cu}^{b/v}$	$D_{Mo}^{f/m}$	$D_{Mo}^{b/v}$
Reduced {Log fO_2 = NNO + 0.6}										
CMA201	Brine	61-62	0.33		29(10)	6.5(3.8)	310 (100)	10 (5)	71 (22)	42 (15)
CMA201	Vapor	3-3.5	0.01	9(4)	0.76(.38)	0.20(0.12)	34 (17)		2.6 (0.8)	
CMA406	Super Critical	12.5-13	0.044	33(4)	3.3(1.2)	0.53(0.21)	310 (83)		8.2 (2.7)	
CMA407	Super Critical	12.5-13	0.044			0.32(0.08)	250 (130)		7.5 (2.4)	
Oxidized { Log fO_2 = NNO + 2 }										
CMA224	Brine	61-62	0.33		13(5)	10(8.3)	175 (60)	20 (11)	130 (66)	31 (21)
CMA224	Vapor	3-3.5	0.01	15(4)	0.6(0.2)	0.31(0.25)	9.2 (3)		4.8 (1.6)	
CMA303	Brine	53-54	0.26	25(6)	11(4)	7.0(5.1)	160 (70)	9 (5)	135 (24)	20 (10)
CMA303	Vapor	5	0.016		0.7(0.1)	0.91(0.74)	18 (9)		6.9 (3.6)	
CMA420	Super Critical	12.5-13	0.044	44(6)	2.1(0.5)	0.92(0.54)	140 (35)		24 (9.8)	
CMA421	Super Critical	12.5-13	0.044			1.8(1.1)	140 (40)		18 (6.4)	

Partition coefficients shown are (f/m)=fluid/melt (vapor, brine or supercritical) and (b/v) = brine/vapor

[m] Total Chloride from Microthermometry (X_{Cl} or X_{NaCleq}), ($CaCl_2$ and $FeCl_2$ counted as 1.5 salinity units)

Figure 1: Experiment Design

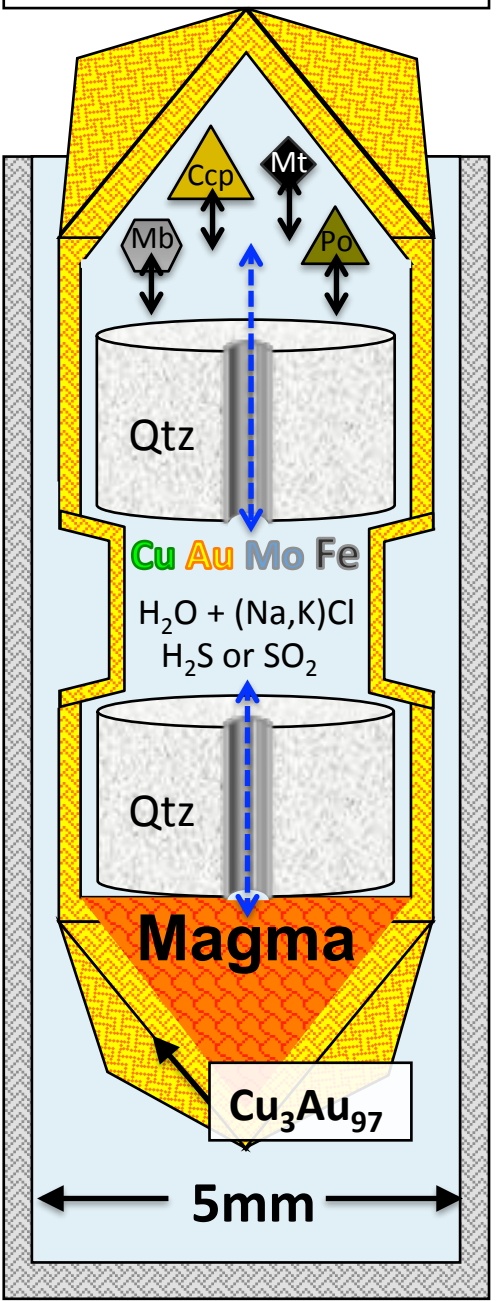

Figure 2: Run-product Glass and Minerals

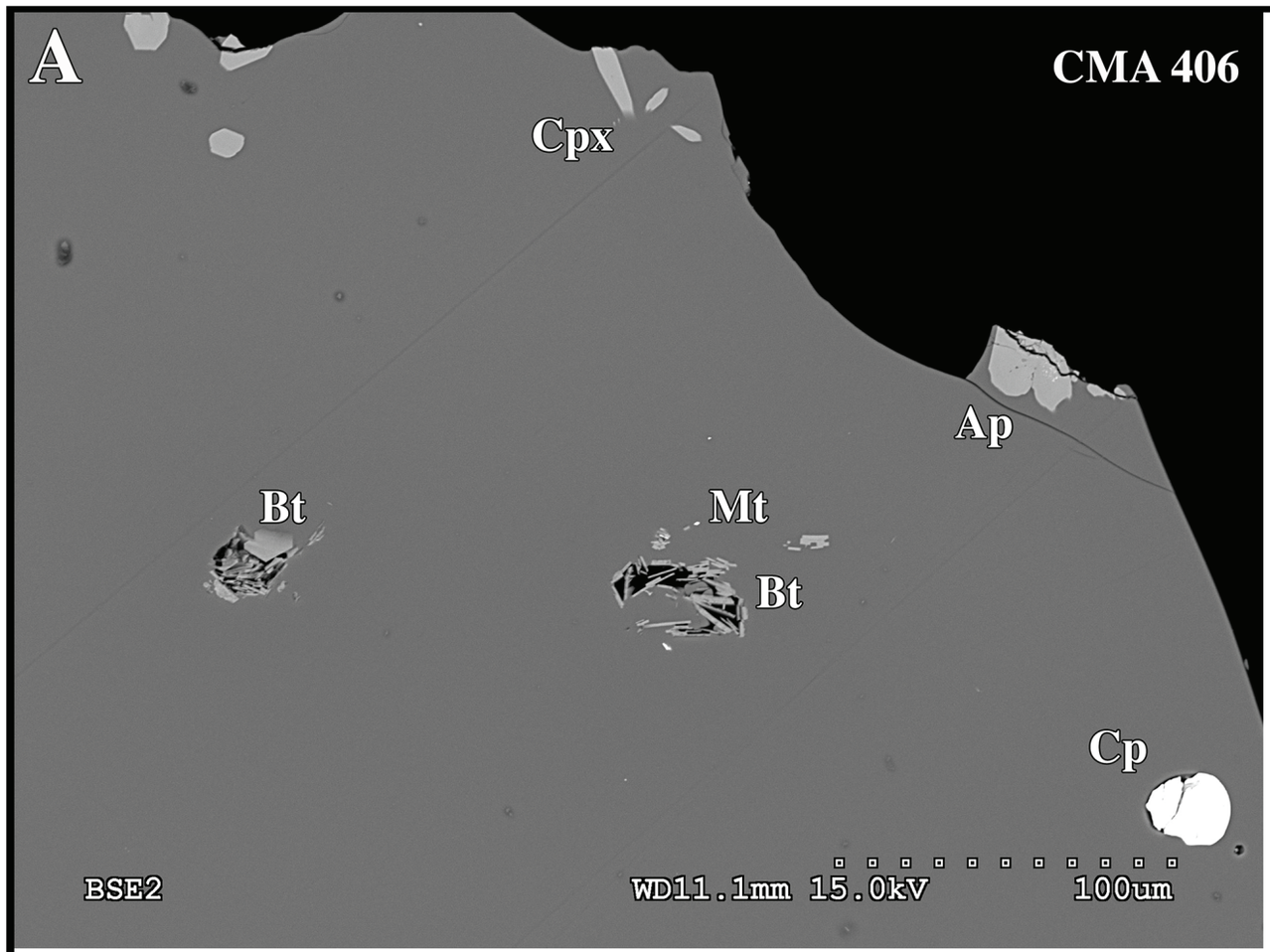

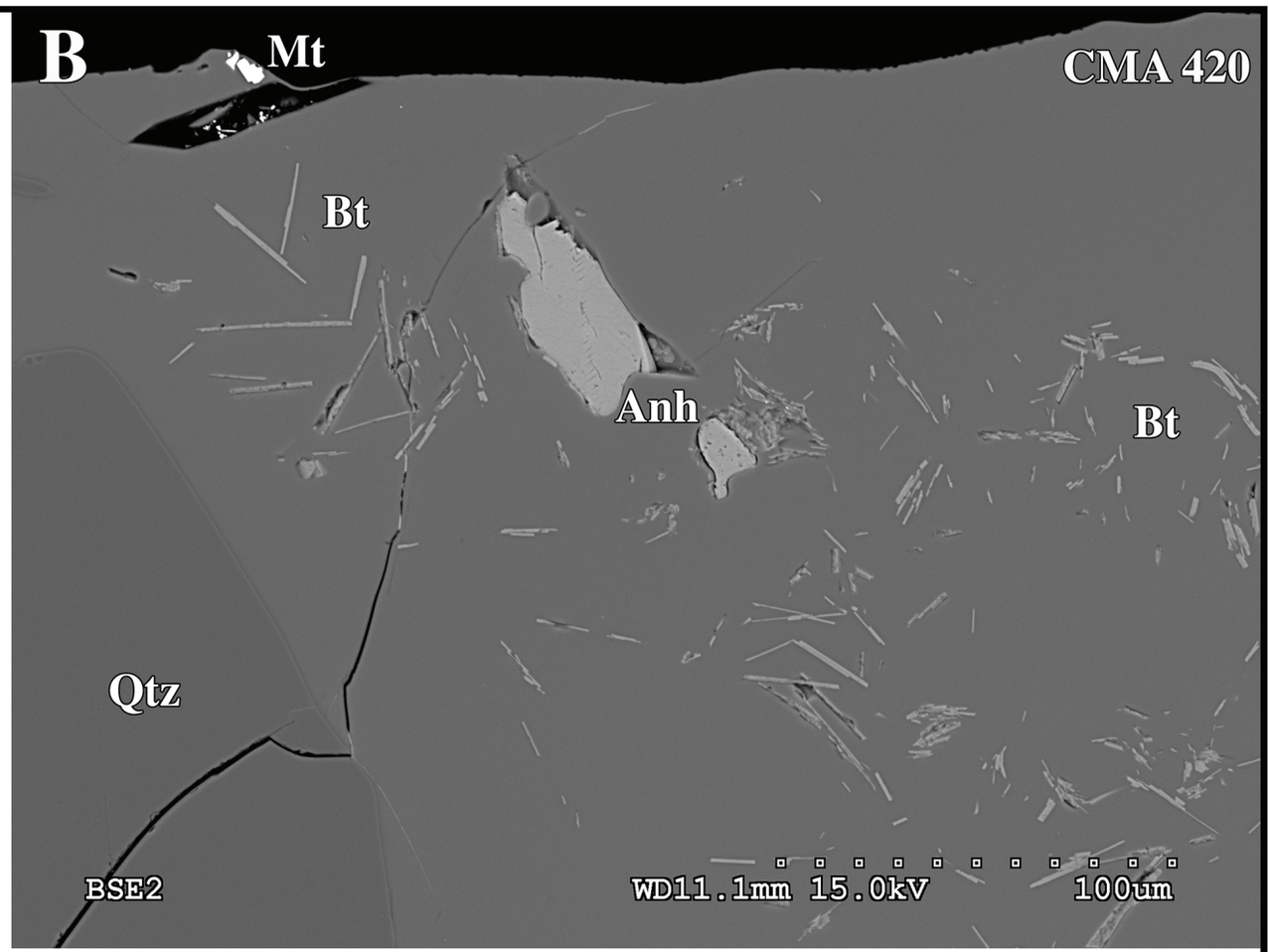

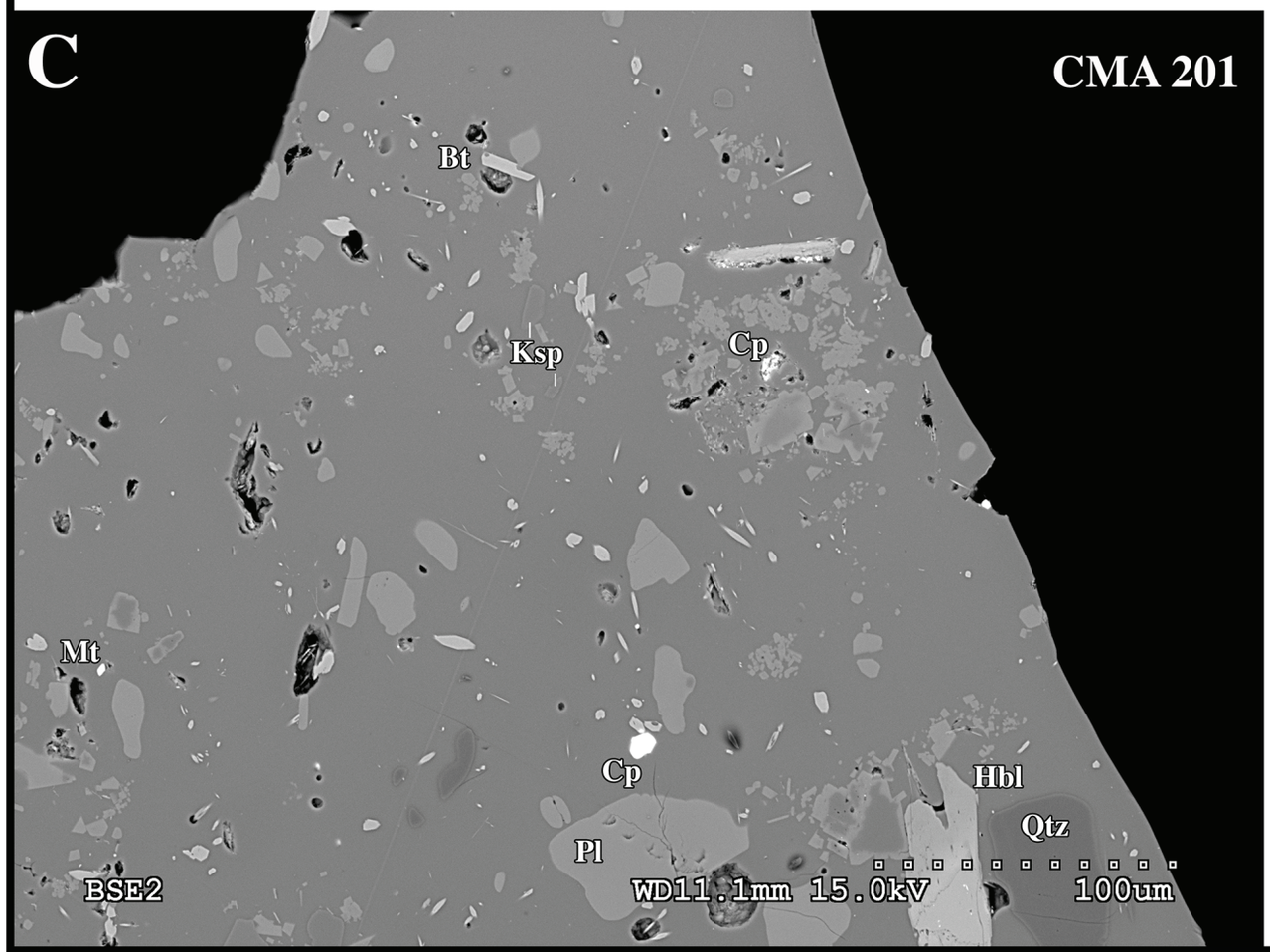

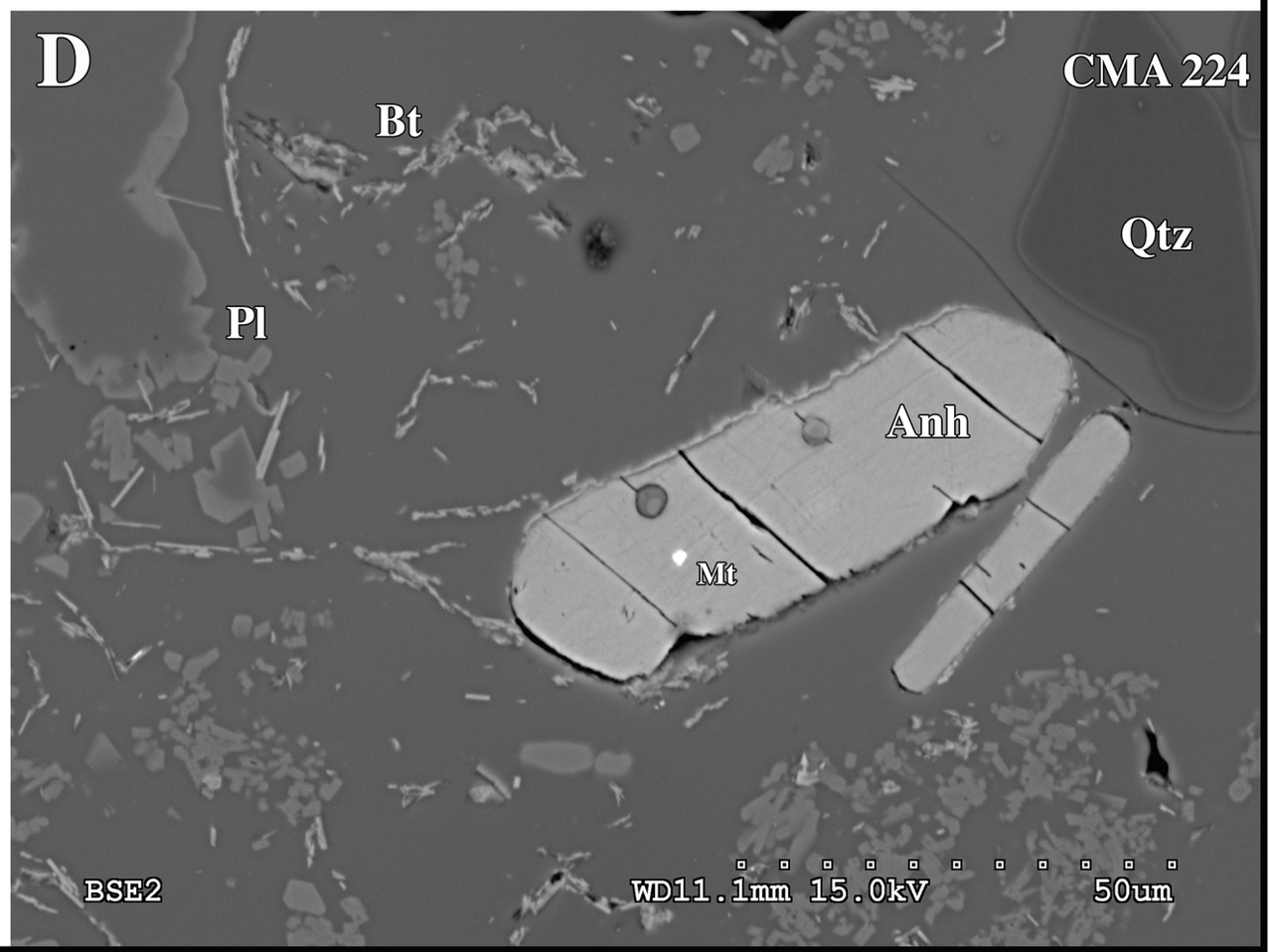

Figure 3: Run-product Fluid Inclusions

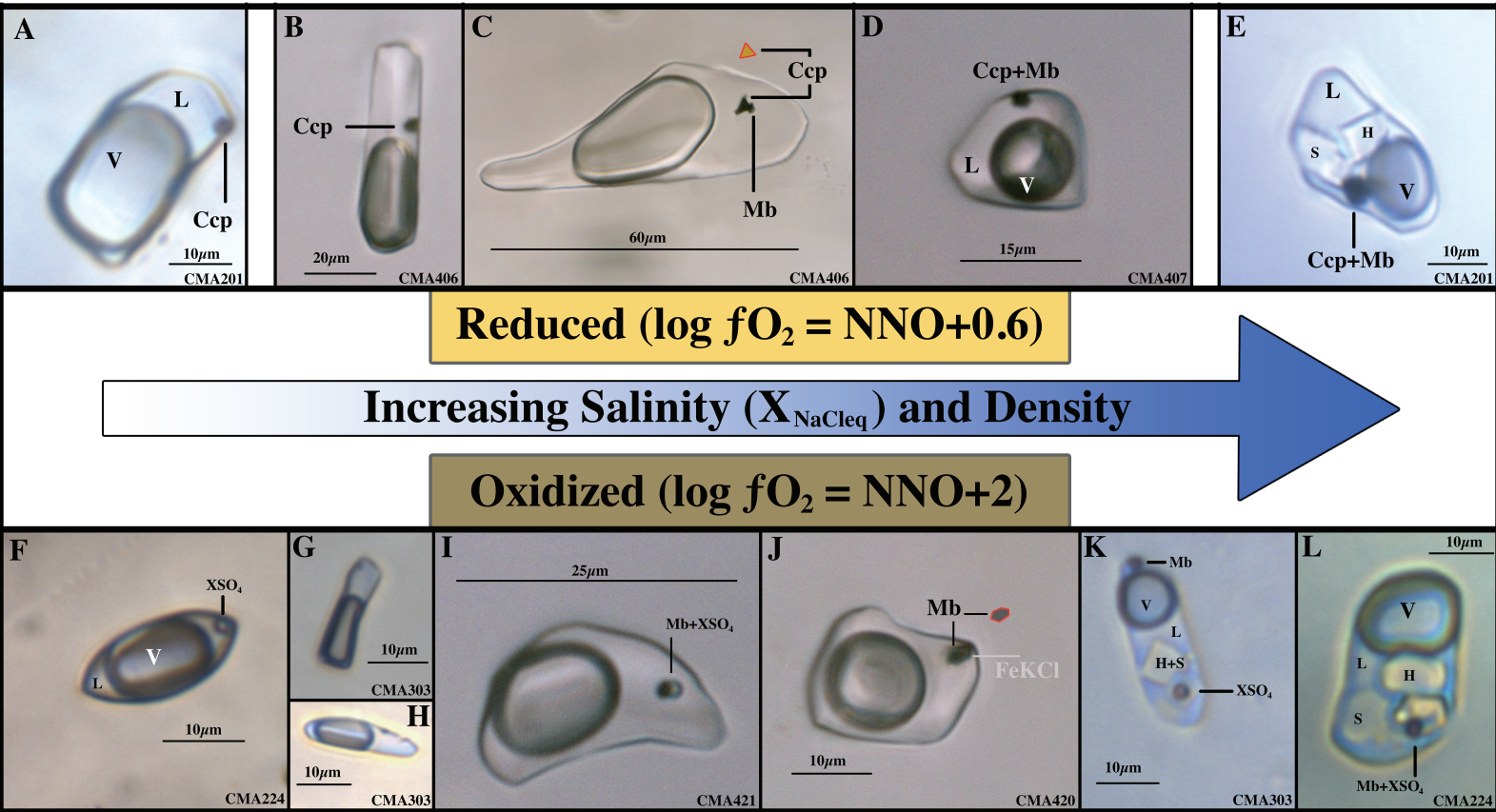

Figure 4: Copper Partitioning (Fluid/Melt) as a function of $X_{NaCl_{eq}}$ and X_{H_2S}

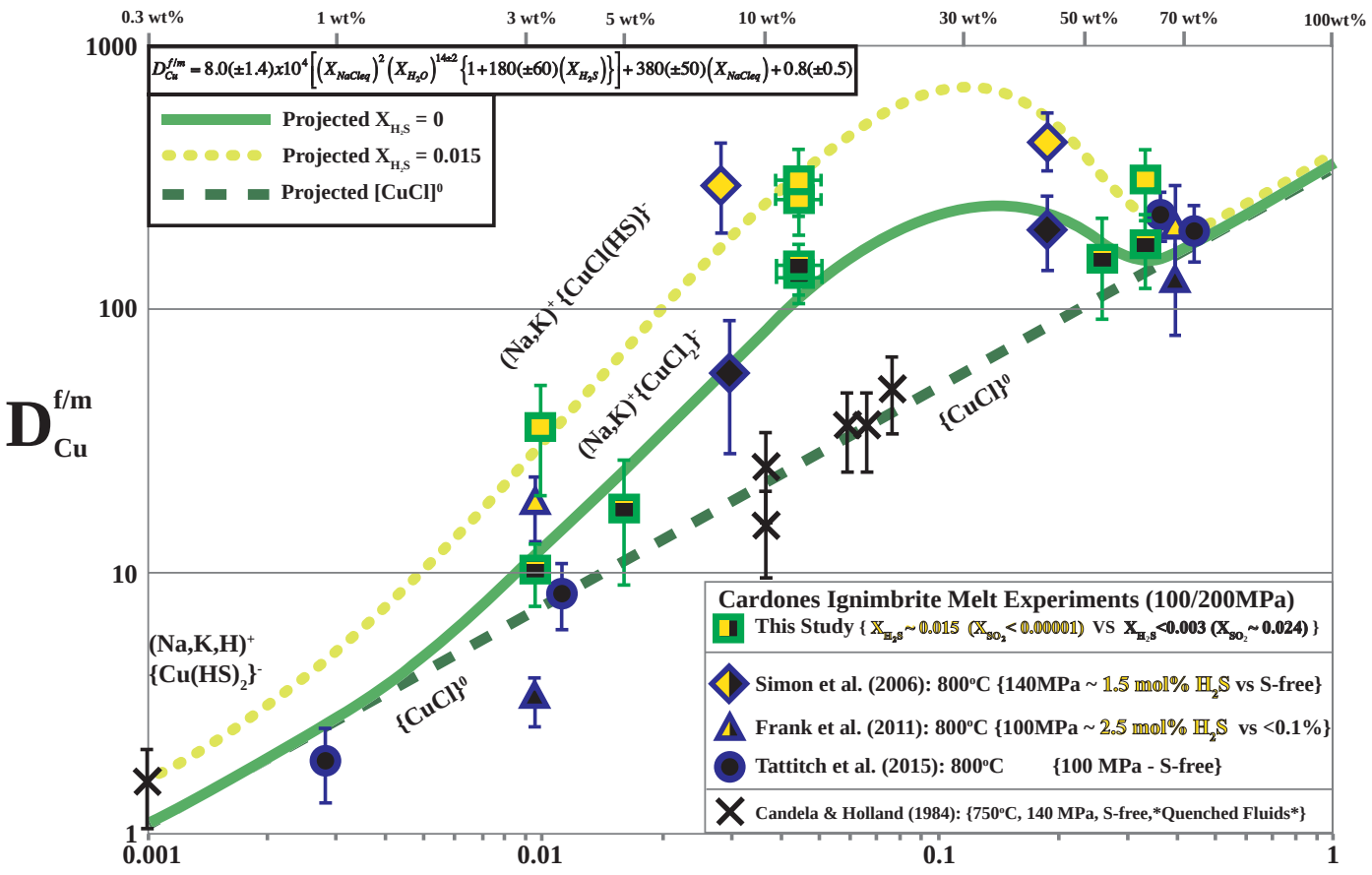

Mole Fraction Chloride ($X_{NaCl_{eq}}$) in Magmatic Volatile Phase

Figure 5: Copper Partitioning (Brine/Vapor) as a function of $D^{b/v}_{Cl}$

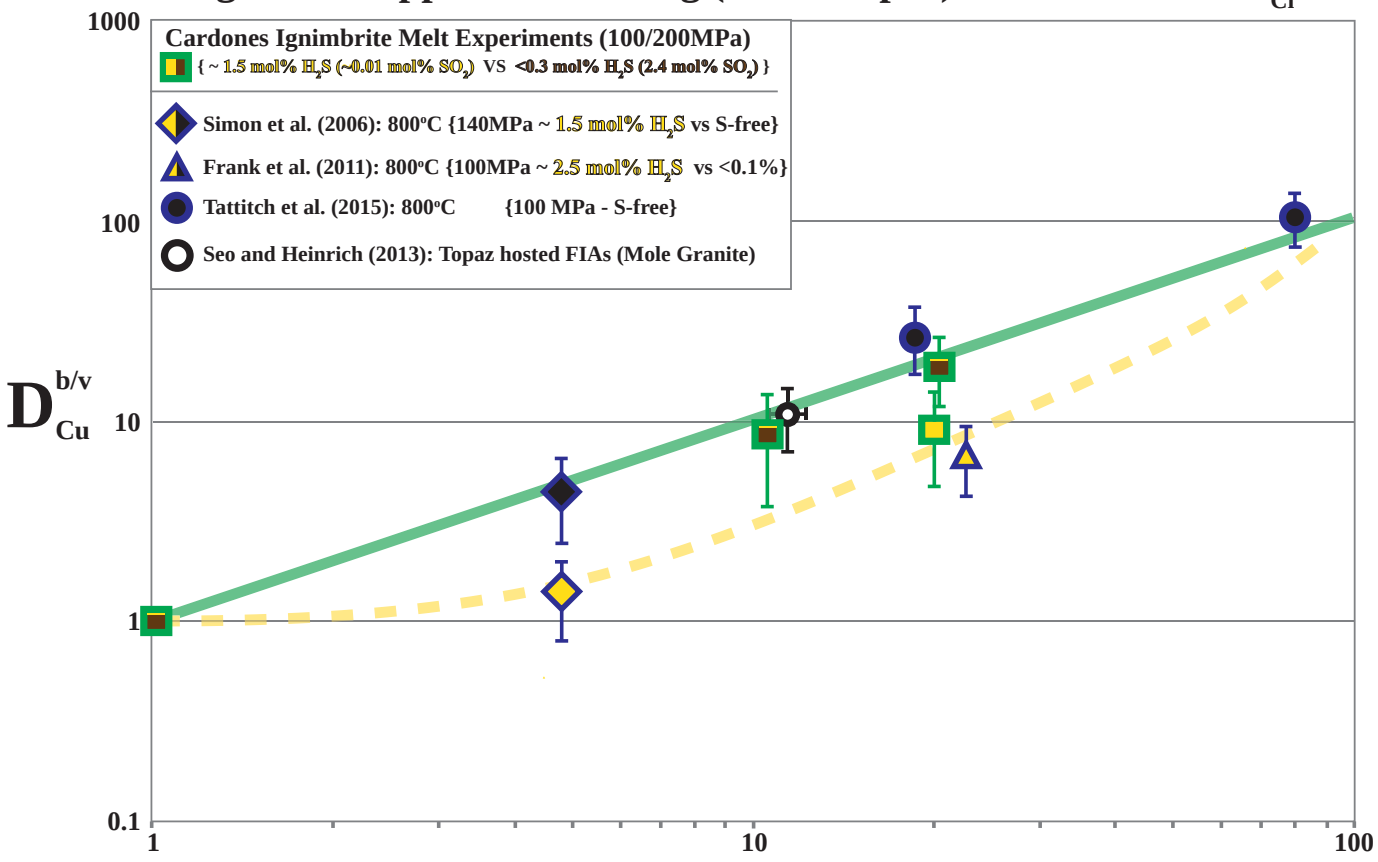

Figure 6: Molybdenum Partitioning (Fluid/Melt) as a function of $X_{NaCl_{eq}}$ and fO_2

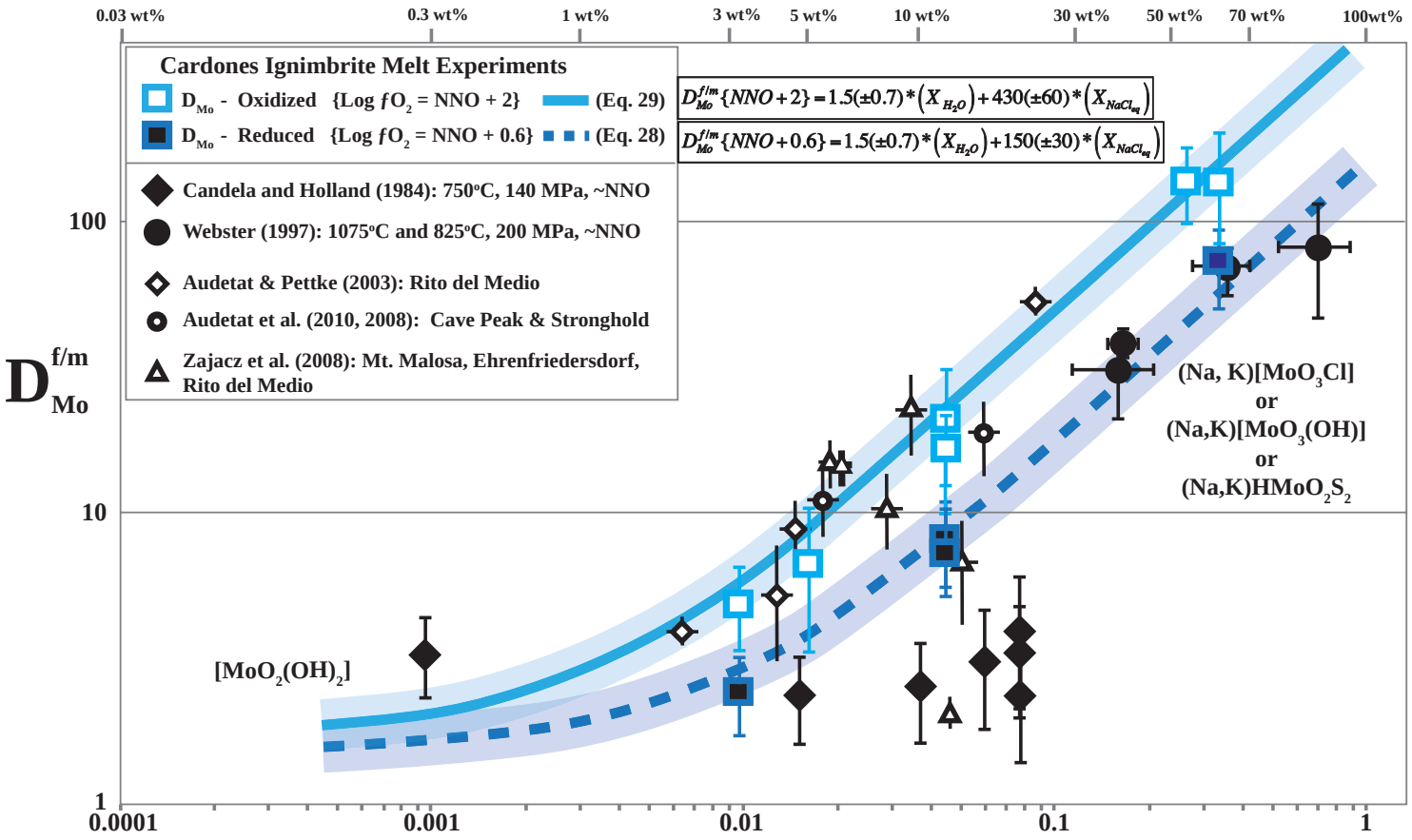

$D^{f/m}_{Mo}$

Mole Fraction Chloride ($X_{NaCl_{eq}}$) in Magmatic Volatile Phase